Available online at www.sciencedirect.com
SCIENCE DIRECT®
Nuclear Instruments and Methods in Physics Research A 503 (2003) 458–484
NUCLEAR INSTRUMENTS & METHODS IN PHYSICS RESEARCH Section A
www.elsevier.com/locate/nima

The Brookhaven muon ($g-2$) storage ring high voltage quadrupoles

Yannis K. Semertzidis[b,*], Gerald Bennett[b], Efstratios Efstathiadis[a], Frank Krienen[a], Richard Larsen[b], Y.Y. Lee[b], William M. Morse[b], Yuri Orlov[c], Cenap S. Ozben[b], B. Lee Roberts[a], Louis P. Snydstrup[b], David S. Warburton[b]

[a] *Department of Physics, Boston University, Boston, MA 02215, USA*
[b] *Brookhaven National Laboratory, Upton, NY 11973, USA*
[c] *Newman Laboratory, Cornell University, Ithaca, NY 14853, USA*

Received 24 July 2002; received in revised form 3 February 2003; accepted 10 February 2003

Abstract

The design, construction, and operation of the electrostatic quadrupoles used in the muon ($g-2$) experiment E821 of BNL are described in detail. A new lead design allowed the construction of a very reliable system which could operate for hundreds of thousands pulses with no sparking. The new design also made possible the elimination of systematic errors associated with the E, B fields generated by the low energy trapped electrons present in Penning traps under medium vacuum conditions.
© 2003 Elsevier Science B.V. All rights reserved.

PACS: 29.20.Dh; 41.85.Lc; 41.20.−q; 39.10+j

Keywords: Storage rings; Muon ($g-2$); Electrostatic quadrupoles; Detection of axial frequency of trapped electrons

1. Introduction

A new storage ring [1,2] has been built at BNL to measure the anomalous magnetic moment of the muon with a sensitivity 20 times better than the last CERN measurement [3]. The principle of the experiment is the same as for the last CERN measurement. The difference ω_a between the spin precession frequency ω_s and the orbital cyclotron frequency ω_c is measured in a homogeneous magnetic field and hence a_μ is determined. The basic equations for the spin precession frequency, the cyclotron frequency and the ($g-2$) frequency are shown below:

$$\omega_s = \frac{eB}{m\gamma} + \frac{e}{m} aB$$

$$\omega_c = \frac{eB}{m\gamma}$$

$$\omega_a = \omega_s - \omega_c = \frac{e}{m} aB$$

with ω_s including both the muon spin precession in its rest frame plus Thomas' precession due to the

*Corresponding author. Tel.: +1-631-344-3881; fax: +1-631-344-5568.
E-mail address: semertzidis@bnl.gov (Y.K. Semertzidis).

0168-9002/03/$ - see front matter © 2003 Elsevier Science B.V. All rights reserved.
doi:10.1016/S0168-9002(03)00999-9

presence of an accelerating frame [4,5]. Polarized muons are stored in the muon storage ring with vertical focusing provided by an electric quadrupole field. The use of electrostatic quadrupoles permits us to have a very uniform magnetic field, which can be measured and monitored with NMR [6,7]. When both electric and magnetic fields are present, and assuming the spin and velocity vectors are orthogonal to the dipole magnetic field, the equation for ω_a becomes

$$\vec{\omega}_a = -\frac{e}{m}\left[a\vec{B} - \left(a - \frac{1}{\gamma^2 - 1}\right)\vec{\beta} \times \vec{E}\right]$$

At the magic gamma, the effect of the electric field on the spin precession and cyclotron frequencies are identical [3]. Hence there is no effect on ω_a. There is a small correction of less than one part per million for off-momentum muons over the 9 cm diameter muon storage region. The muon magic momentum is:

$$p_\mu = \frac{m_\mu}{\sqrt{a_\mu}} = 3.094 \text{ GeV}/c$$

corresponding to a radius of $R_0 = 7112$ mm for a uniform magnetic field of $B \approx 1.45$ T.

The cross section of the muon storage ring showing the C-shaped iron yoke, magnet coils, and vacuum chamber are shown in Fig. 1. The electrostatic quadrupoles are visible inside the chamber in the magnet gap.

2. Lattice design

In a storage ring with dipole magnetic field B_0 and electric gradient $\partial E_R/\partial R$, the field index n is defined as

$$n(s) = \frac{R}{\beta B}\frac{\partial E_R(s)}{\partial R}, \quad \beta = u/c \tag{1}$$

where s is the longitudinal coordinate, so $\phi = s/R$ is the azimuth. In the linear approximation the horizontal (radial), x, and vertical, y, betatron oscillations are described in the usual way (For a more complete description of the beam dynamics in the $(g-2)$ ring see Ref. [9].) [8,9],

$$x = x_e + \sqrt{\varepsilon_x \beta_x(s)}\cos\left[\nu_x \frac{s}{R} + \phi_x(s)\right] \tag{2}$$

$$y = \sqrt{\varepsilon_y \beta_y(s)}\cos\left[\nu_y \frac{s}{R} + \phi_y(s)\right] \tag{3}$$

$$x_e(s) = R_e(s) - R_0 = D(s)\frac{p - p_0}{p_0}, \quad cp_0 = eBR_0 \tag{4}$$

where radius R_0 and momentum p_0 correspond to the center, in the transverse plane, of the electric quadrupoles and the vacuum chamber. In this center, the electric field equals zero. $\beta_{x,y}$ are the betatron beta-functions, measured in meters, see Table 3 below, and $\sqrt{\varepsilon_{x,y}}$ are amplitude factors in the equations for the trajectories of individual particles. $D(s)$, $\beta_{x,y}(s)$ and $\phi_{x,y}(s)$ are periodic functions, almost constant in the BNL $(g-2)$ ring; their period, in this case, equals $L/4 \equiv \pi R/2$. Every muon oscillates around its own equilibrium radius $R_s(s)$ defined by its momentum, p.

For the CERN experiment the quadrupole electrodes occupied 72% of the total circumference. There was a gap at the location of the inflector magnet, which cancels the magnetic field for the incoming beam and another gap on the opposite side of the ring to preserve the lattice symmetry. The E821 lattice is shown in Fig. 2. There are four quadrupole regions which are shown as Q_1, Q_2, Q_3, and Q_4. E821 was performed with both muon injection and pion injection. Muon injection requires a kicker magnet which kicks the beam onto a stable trajectory [10]. The pion decay provides the kick for pion injection. Muon injection is much more efficient, with the background associated with injection being much smaller. The kicker magnet must be about 90° from the inflector magnet. Therefore space must be left for both the inflector and kicker magnets with two other gaps at 180° and 270° to preserve the lattice symmetry. The electrodes occupy only 43% of the total circumference for the BNL lattice. The electric field gradient must be 1.7 times greater than the CERN design for the same average field index. However, the higher symmetry has two beneficial results: the beta functions are much more uniform around the azimuth and the orbit stability is better.

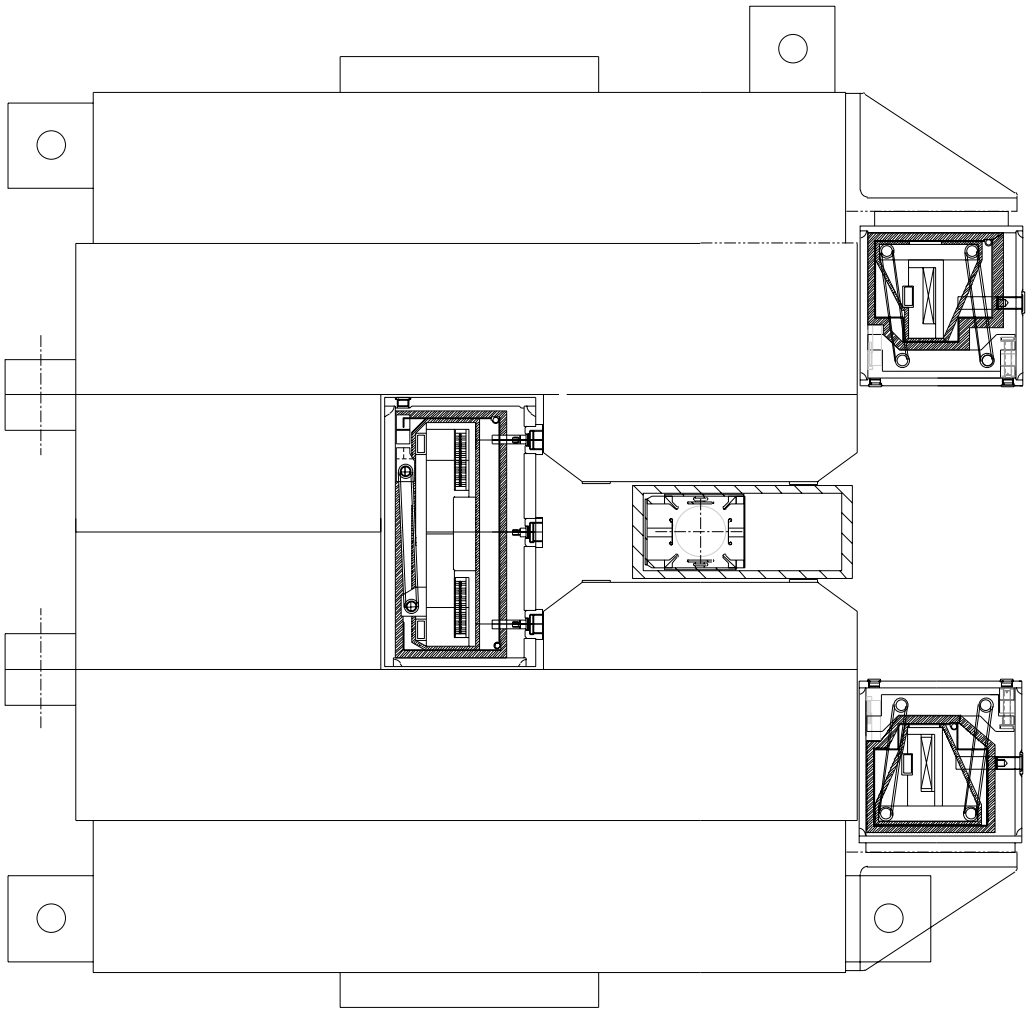

Fig. 1. The cross section of the muon storage ring showing the magnet pole pieces, the three cryostats housing the corresponding superconducting coils, and the vacuum chamber in between the pole pieces housing the electrostatic quadrupoles.

The Fourier analysis of the CERN and BNL lattices $F(s/R) = \sum A_N \cos(Ns/R)$ up to $N = 12$ is shown in Table 1.

Note that the BNL lattice design with the four-fold symmetry has no $N = 2$ term which drives the strong octupole resonance with two-fold symmetry. The minimum and maximum beta functions are shown in Table 2 for two, four, and eight-fold symmetry.

The period $\pi R/2$ with this four-fold symmetry is much less than the period of the radial oscillations (close to $2\pi R$), and especially the period of the vertical betatron oscillations ($\sim 6\pi R$). For this reason we can, with a very good accuracy, use in most estimates the field index n averaged over the orbit, $n = \langle n(s) \rangle$. In our case, $n = 0.43n_0$, where n_0 is the n-value as defined in Eq. (1) inside the quadrupole region. In this "smoothed" approximation, the betatron tunes (the number of oscillations during one turn) are defined as $\nu_x = \sqrt{1-n}$, $\nu_y = \sqrt{n}$, and $\langle D(s) \rangle = \alpha R_0$, $\alpha = 1/(1-n)$, $\beta_x = R/\nu_x$, $\beta_y = R/\nu_y$, the familiar weak focusing formulas; both $D(s)$ and $\beta_{x,y}(s)$ are constant. In reality, they slightly change along s, with $D(s)$, $\beta_x(s)$ maximal in the middle of intervals between quads and minimal in the

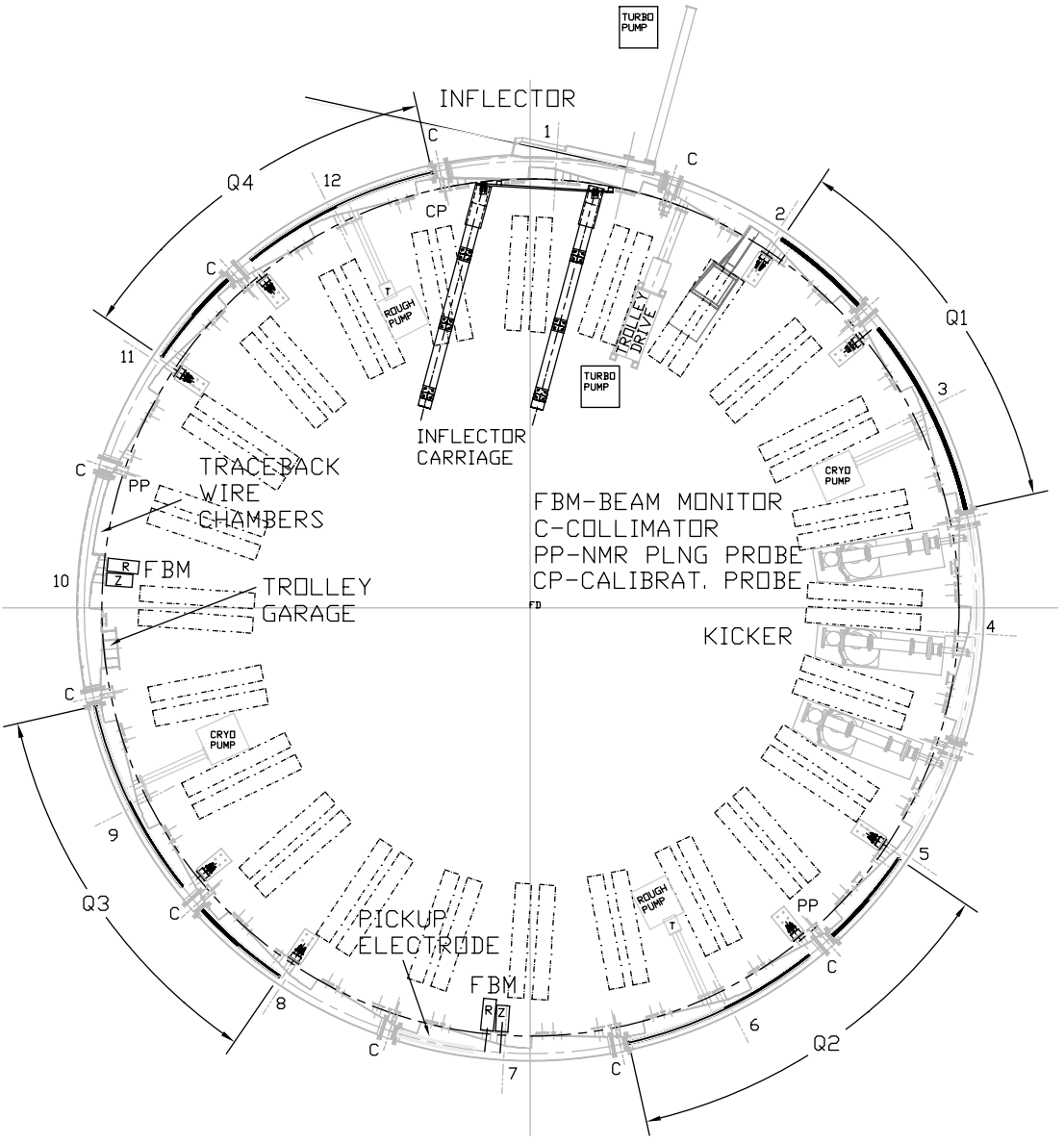

Fig. 2. The muon ($g-2$) ring lattice with a radius of $R_0 = 7112$ mm. The muon storage region is a torus of radius $R_0 = 7112$ mm and a cross section diameter of 90 mm. The quadrupole regions are denoted as Q_1, Q_2, Q_3, and Q_4. The 24 sets of detector rails are shown as dashed lines.

middle of quads, and $\beta_y(s)$, inversely, minimal and maximal at these azimuths. Using the following formulas we show in Tables 3 and 4 the actual values of the betatron parameters for a range of n-values relevant to our muon ($g-2$) experiment.

$$\cos(\pi\nu_x/2) = \cos(l_i/R)\cos(\sqrt{1-n_0}\,l_q/R) - \frac{1}{2}\left(\sqrt{1-n_0} + \frac{1}{\sqrt{1-n_0}}\right) \times \sin(l_i/R)\sin(\sqrt{1-n_0}\,l_q/R) \quad (5)$$

Table 1
Fourier amplitudes A_N of the CERN and BNL lattice

N	CERN	BNL E821
0	0.72	0.43
2	0.25	0
4	0.15	0.58
6	0.05	0
8	0.03	0.05
10	0.06	0
12	0.04	0.22

Table 2
Beta functions for two, four and eight-fold lattice symmetry

N	2	4	8
β_x(max)	24.4m	7.9m	7.7m
β_x(min)	2.30m	7.35m	7.6m
$\sqrt{\text{max/min}}$	3.26	1.04	1.01
β_y(max)	21.8m	19.9m	19.5m
β_y(min)	16.8m	18.8m	19.2
$\sqrt{\text{max/min}}$	1.15	1.03	1.01

The minimum and maximum values of the beta functions are much closer with the four-fold symmetry used in E821 than with the two-fold symmetry of CERN.

$$\cos(\pi\nu_y/2) = \cos(\sqrt{n_0}\,l_q/R) - \frac{\sqrt{n_0}\,l_i}{2R}\sin(\sqrt{n_0}\,l_q/R) \tag{6}$$

$$\beta_{x,\min}/R = -w + \sqrt{w^2 + 1/(1-n_0)}$$
$$w = \frac{n_0}{2(1-n_0)}\frac{\sin(l_i/R)}{\sin(\pi\nu_x/2)} \tag{7}$$

$$\beta_{x,\max}/R = u + \sqrt{u^2+1}$$
$$u = \frac{n_0}{2\sqrt{1-n_0}}\frac{\sin(\sqrt{1-n_0}\,l_q/R)}{\sin(\pi\nu_x/2)} \tag{8}$$

$$\beta_{y,\min}/R = \frac{\sin(\pi\nu_y/2)}{\sqrt{n_0}\sin(\sqrt{n_0}\,l_q/R)} \tag{9}$$

$$\beta_{y,\max}/R = r + \sqrt{r^2 + 1/n_0}$$
$$r = \frac{l_i}{2R\sin(\pi\nu_y/2)} \tag{10}$$

$$D_{\min}/R = \frac{1}{1-n_0} - \frac{((D_{\max}/R)-1)\sin(l_i/2R)}{\sqrt{1-n_0}\sin(\sqrt{1-n_0}\,l_q/2R)} \tag{11}$$

$$D_{\max}/R = 1 + \frac{n_0}{(1-n_0)\cos(l_i/2R) + \sqrt{1-n_0}\sin(l_i/2R)\cot(\sqrt{1-n_0}\,l_q/2R)}. \tag{12}$$

Here l_i is the length of the interval between quadrupoles, $l_i/R = 0.895354$ in our experiment. l_q is the length of a quadrupole, $l_q/R = 0.675442$, n_0 is the field index inside the electric quadrupoles, $n_0 = n/0.43$.

In this table, we have omitted a strongly resonant value $n = 0.126$, see Figs. 3 and 4. The six-digit precision in the frequency is necessary because we need to know all essential combinatorial resonances, including very high multipole resonances, in both beam and spin dynamics.

3. Electrode design

The equipotential lines for a quadrupole potential lie on hyperbolae. Therefore, the electrodes should ideally have a hyperbolic shape. In a real design, however, the limited extent of the electrodes and the vacuum chamber walls at ground potential produce higher order multipoles. The E821 electrode design is shown in Figures 5 and 6. Flat electrodes have higher normal multipoles b_6, b_{10}, the amplitudes of the 12-pole and 20-pole correspondingly (see Section 6), etc. The width of the electrode can be adjusted to make b_6 near zero. When this is done, $b_{10}/b_2 \approx 1.9\%$ at the edge of the circular aperture. It also turns out that the quadrupole component, for the flat plate geometry used, is higher by $\sim 4\%$ at $r = 50$ mm, the location of the center of the plates, than if the plates were of hyperbolic shape. For the complete list of

Table 3
The modified (average values over the ring) ν_x, ν_y, and the $\beta_{x,\min,\max}/R$, $\beta_{y,\min,\max}/R$ values due to the discrete nature of the quadrupole coverage of the $(g-2)$ ring

n	$\sqrt{n}$	ν_y	$\sqrt{1-n}$	ν_x	$\beta_{y,\min}/R$	$\beta_{y,\max}/R$	$\beta_{x,\min}/R$	$\beta_{x,\max}/R$
0.120	0.346410	0.347840	0.938083	0.938732	2.8159	2.9414	1.0357	1.0936
0.121	0.347851	0.349298	0.937550	0.938209	2.8037	2.9297	1.0361	1.0944
0.122	0.349285	0.350750	0.937017	0.937689	2.7916	2.9181	1.0364	1.0953
0.123	0.350714	0.352197	0.936483	0.937166	2.7796	2.9067	1.0368	1.0961
0.124	0.352136	0.353638	0.935949	0.936643	2.7678	2.8954	1.0371	1.0969
0.125	0.353553	0.355074	0.935414	0.936120	2.7561	2.8843	1.0375	1.0978
0.127	0.356371	0.357930	0.934345	0.935074	2.7332	2.8624	1.0382	1.0995
0.128	0.357771	0.359348	0.933809	0.934550	2.7219	2.8517	1.0385	1.1003
0.129	0.359166	0.360762	0.933274	0.934027	2.7107	2.8411	1.0389	1.1012
0.130	0.360555	0.362170	0.932738	0.933521	2.6997	2.8306	1.0392	1.1020
0.131	0.361939	0.363574	0.932202	0.932979	2.6888	2.8202	1.0396	1.1030
0.132	0.363318	0.364972	0.931665	0.932454	2.6780	2.8100	1.0399	1.1037
0.133	0.364692	0.366365	0.931128	0.931930	2.6674	2.7999	1.0403	1.1046
0.134	0.366060	0.367752	0.930591	0.931405	2.6568	2.7898	1.0406	1.1054
0.135	0.367423	0.369135	0.930054	0.930898	2.6464	2.7800	1.0410	1.1063
0.136	0.368782	0.370513	0.929516	0.930441	2.6361	2.7702	1.0413	1.1071
0.137	0.370135	0.371886	0.928978	0.929829	2.6259	2.7605	1.0417	1.1080
0.138	0.371484	0.373253	0.928440	0.929303	2.6158	2.7510	1.0421	1.1089
0.139	0.372827	0.374617	0.927901	0.928778	2.6058	2.7415	1.0424	1.1097
0.140	0.374166	0.375975	0.927362	0.928250	2.5959	2.7321	1.0428	1.1106

Table 4
The maximum and minimum values of $D(s)$, see text, as a function of n-value

n	0.121	0.123	0.125	0.127	0.129	0.131	0.133	0.135	0.137	0.139
$D_{\min}/R$	1.124	1.126	1.128	1.130	1.132	1.134	1.137	1.140	1.142	1.144
$D_{\max}/R$	1.148	1.151	1.154	1.157	1.160	1.163	1.165	1.168	1.171	1.174

multipoles in the quadrupole region under various conditions see Section 6.

A tracking study was done to evaluate the betatron modulation with flat electrodes. This result is in agreement with the analytical calculations described above and give acceptable betatron amplitude modulation. The flat design was adopted as it was felt these electrodes would be easier to fabricate and the overall tolerances on construction and alignment would be less with flat vs. hyperbolic electrodes. The effects of the vacuum chamber walls are minimized by the rails which have the quadrupole symmetry. The NMR beam-tube trolley uses the rails to travel around the ring. It carries a matrix of 17 NMR probes, which maps the magnetic field in the muon storage region [11].

4. Electrode construction

The design, materials used, and the construction method of the quadrupoles are described next.

4.1. Quadrupole electrodes

4.1.1. Quadrupole segments

There are four symmetrically located quadrupole regions. Each region consists of an electrode azimuthal length of 39°, which is installed in

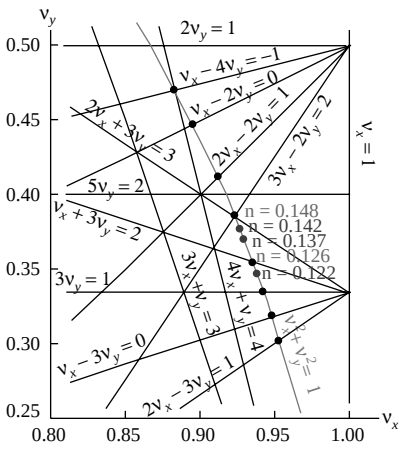

Fig. 3. The muon $(g-2)$ ring tune plane with the three n-values used to run the experiment. There are two strong resonances, at $n = 0.126$ and 0.148 near the operating values of $n = 0.122$, 0.137, and 0.142. Due to the discrete nature of the quadrupole structure the modified averaged ν_x and ν_y do not satisfy the condition $\nu_x^2 + \nu_y^2 = 1$ but is slightly greater than 1, see Table 3, resulting in slightly different resonance values than shown here. The n-value and the frequency f_{cbo} of the coherent betatron oscillations [1] are related to the voltage V on the quad plates with the following approximate equations: $n \approx 5.6 \times 10^{-6} \times V$, and $f_{cbo} \approx 19.36 \times V$, where f_{cbo} is in Hz and V in Volts. As an example a voltage of ± 25.3 kV on the quadrupole plates corresponds to $n \approx 0.142$ and $f_{cbo} \approx 490$ kHz.

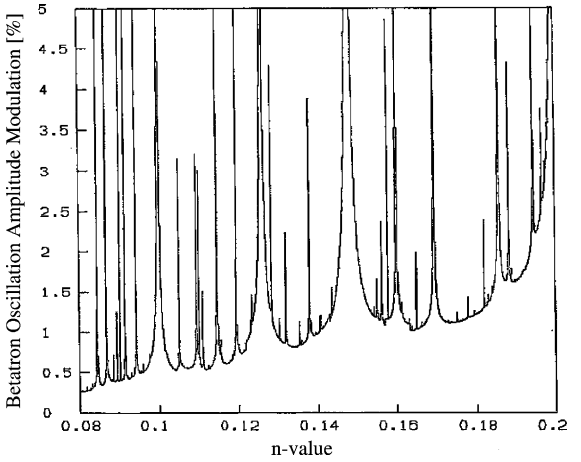

Fig. 4. The result of the analytic calculation of the betatron oscillation amplitude modulation in % due to resonances present in the $(g-2)$ ring as a function of n-value. The E-field multipoles, which are driving the resonances, are mainly due to the geometry of the plates and the electrode alignment errors. The resonances at $n = 0.126$ and 0.148 are clearly visible.

two 28° vacuum chambers, as shown in Fig. 7. A 13° electrode segment is located in the upstream chamber and a 26° electrode is in the next downstream chamber. The basic electrode is made in 13° lengths (an average of 1.6 m long at 7.112 m storage ring radius) to improve the positioning accuracy and to lower manufacturing costs.

4.1.2. *Upper and lower electrodes*

The upper and lower electrodes shown in Fig. 5 are CNC machined from 3 mm, grade 6061-T6 aluminum plate. Even though aluminum is not the preferred material for a high voltage component it was thought to be the best because of its low magnetic susceptibility [12] of $+16.5 \times 10^{-6}$ in cgs units as compared to titanium of $+153 \times 10^{-6}$. The titanium plates were found to exceed the specifications of the magnetic field quality, whereas those made of aluminum were acceptable.

4.1.3. *Inner and outer electrodes*

The inner and outer electrodes shown in Fig. 5 are 0.5 mm thick (except the Q1 outer-see below), grade 5052-H34 aluminum. The aluminum is found to not substantially deteriorate the electromagnetic calorimeter [13] energy resolution. The electrodes were formed in the flat condition using a special die which provided high dimensional accuracy and preserved the mill surface finish. The electrodes were then curved to the approximate storage ring radius by hand to a template, then held to a more accurate radius by supports during mounting.

4.1.4. Q_1 *outer electrode*

The four quadrupole regions are similar with one exception. The outer electrodes in the Q_1 region are 0.10–0.13 mm thick (except the rolled places and the region around the insulators in order to provide support strength to the plates), less than the normal 0.5 mm found on the inner and outer electrodes in the other regions. The Q_1 location is such that the incoming beam has to go through the outer Q_1 electrode. The particles (pions or muons) will multiple scatter and lose energy on both the electrode and their supporting

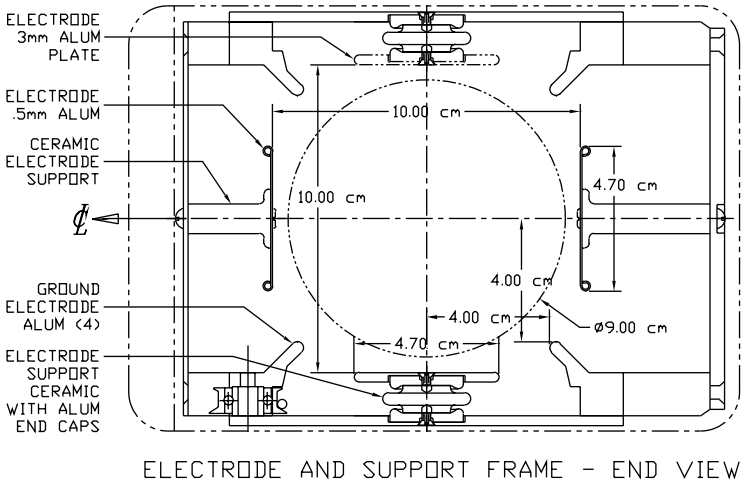

Fig. 5. The cross section of the quadrupole plates (“electrodes”) and NMR trolley rails (“ground electrodes”). The top-bottom as well as the left-right high voltage support insulators are also shown.

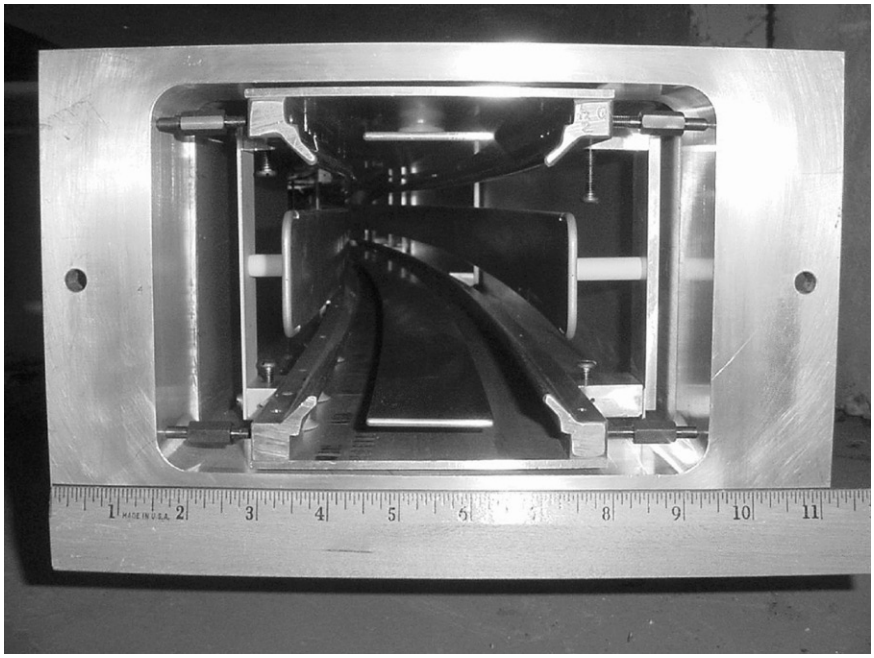

Fig. 6. A photograph taken from the end of a vacuum chamber housing the quadrupole plates; the ring center is on the left. The distance between quadrupole plates at equal potential is 10 cm. The bottom left and the top right rails are where the cable NMR trolley rides when measuring the magnetic field. The other two rails were used to keep the symmetry in the quadrupole region. The ruler units are in inches.

high voltage insulator. It was therefore very important to make those electrodes (Q_1 full and Q_1 half) as thin as possible and yet sturdy enough so that they do not buckle.

4.1.5. Leads

The typical leads arrangement for each set of four electrodes are shown in Fig. 8. The leads are 3 mm O.D. aluminum tube with 0.5 mm

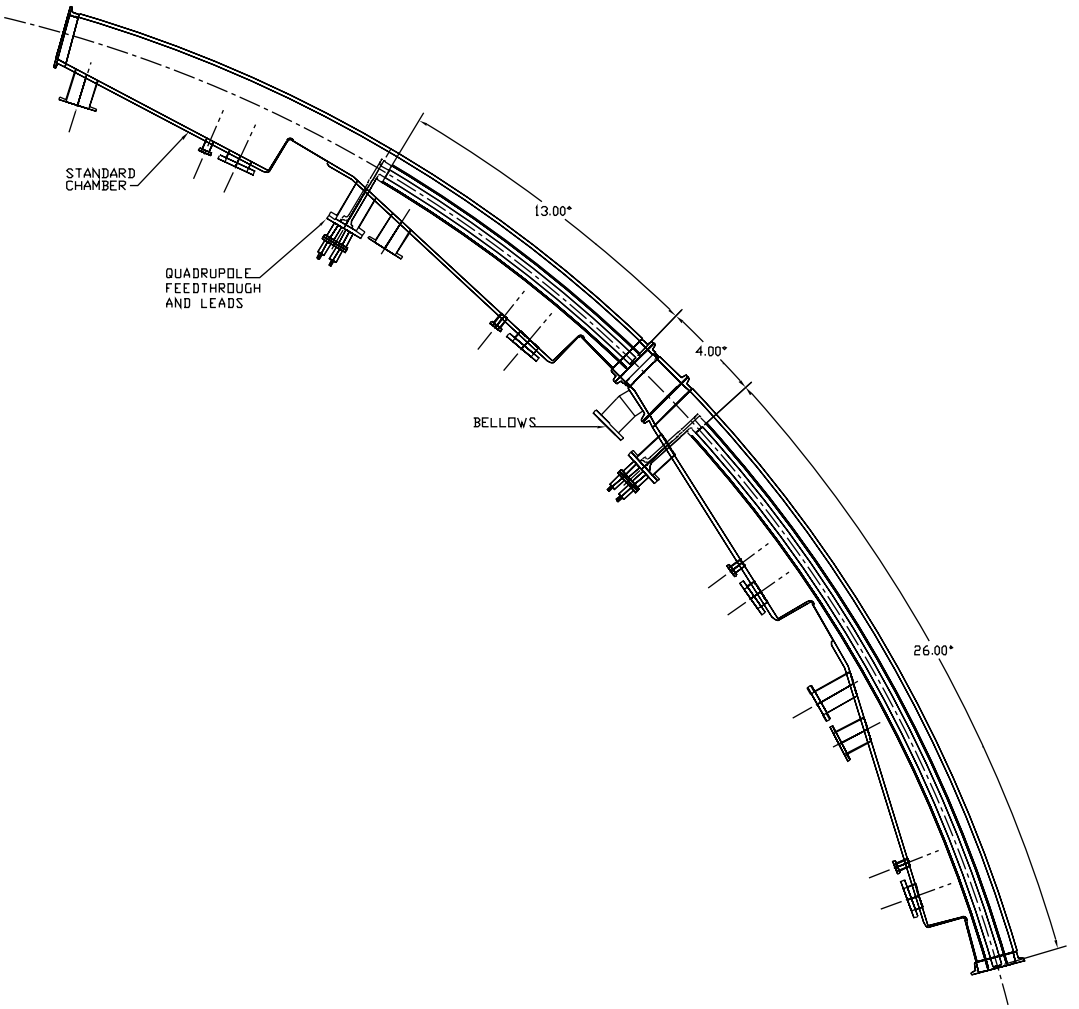

Fig. 7. Two consecutive vacuum chambers housing a quadrupole section. The upstream chamber houses the short section with a length of 13° and the downstream houses the long section with a length of 26°.

wall-thickness with small drilled holes to eliminate virtual vacuum leaks. The air to vacuum feedthroughs are a standard 30 kV commercial design. Tube-to-electrode joints and tube-to-tube joints are made with 2 mm aluminum pins.

4.2. Quadrupole mounting and support

4.2.1. Support frame

Each 13° electrode is mounted at three support points to a 28° aluminum support frame. A plan view of the support frame is shown in Fig. 9. The upper and lower plates of the frame were CNC machined to the storage ring radius. The rigidity of the frame comes primarily from the corner ground plane electrodes: two screwed to the upper plate and two to the lower plate. These ground electrodes were extruded shapes which were stretch-formed to the approximate radius. Fifteen bars join the upper and lower assemblies. The support frame was accurately assembled on a flat surface.

Two of the support frame ground electrodes also serve as rails for a trolley containing the NMR magnet field measurement probes. The inner, lower rail has guide wheels for the trolley drive cable, visible in Fig. 6.

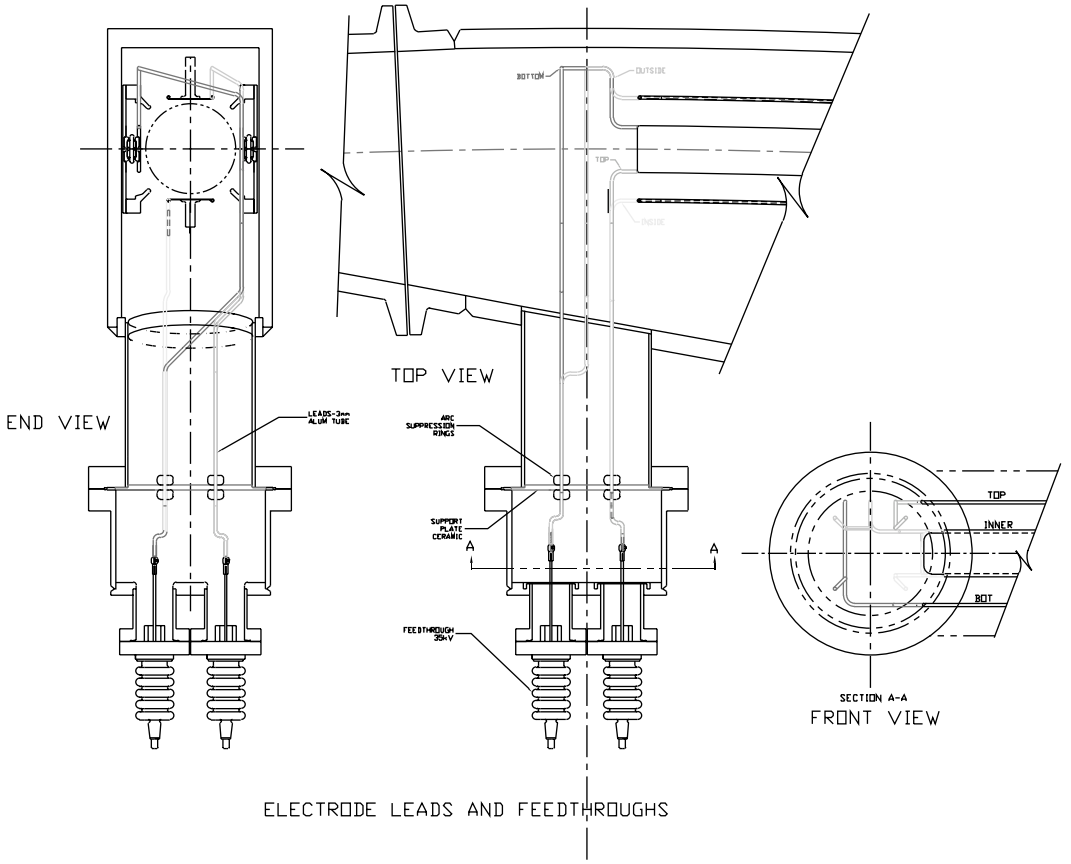

Fig. 8. The leads connected with the quadrupole plates are shown in different views. The maximum azimuthal extent of the leads is less than 10 cm from the end of the plates. The high voltage feedthroughs are also shown.

4.2.2. Electrode mounting

Each 13° electrode is attached to the support frame at three points using electrical isolators. The isolators for the upper and lower electrodes are made of Macor ceramic bonded to aluminum end plates, see Fig. 5. The upper and lower electrodes are 1.1 cm from the closest ground surface. The inner and outer electrode isolators were also machined from Macor.

4.3. Electrode alignment

The alignment of the quadrupole electrodes was performed in the following steps:

(1) Upper and lower electrodes were aligned relative to the accurately CNC machined inside diameter of the support frame plate. Inner and outer electrodes are vertically aligned relative to the lower electrode. The flexible inner and outer sheet metal electrodes are shimmed into the correct radius relative to the upper and lower electrode radial position. Acrylic gauge blocks were made for these alignments.

(2) The vacuum chamber is "characterized" geometrically using a computer interfaced theodolite system (i.e., ManCAT). The chamber end flanges and targets on the inside radius define an external reference for the chamber dimensional database.

(3) The support frame is installed into the vacuum chamber relative to the chamber end flanges. Adjusting screws on the frame

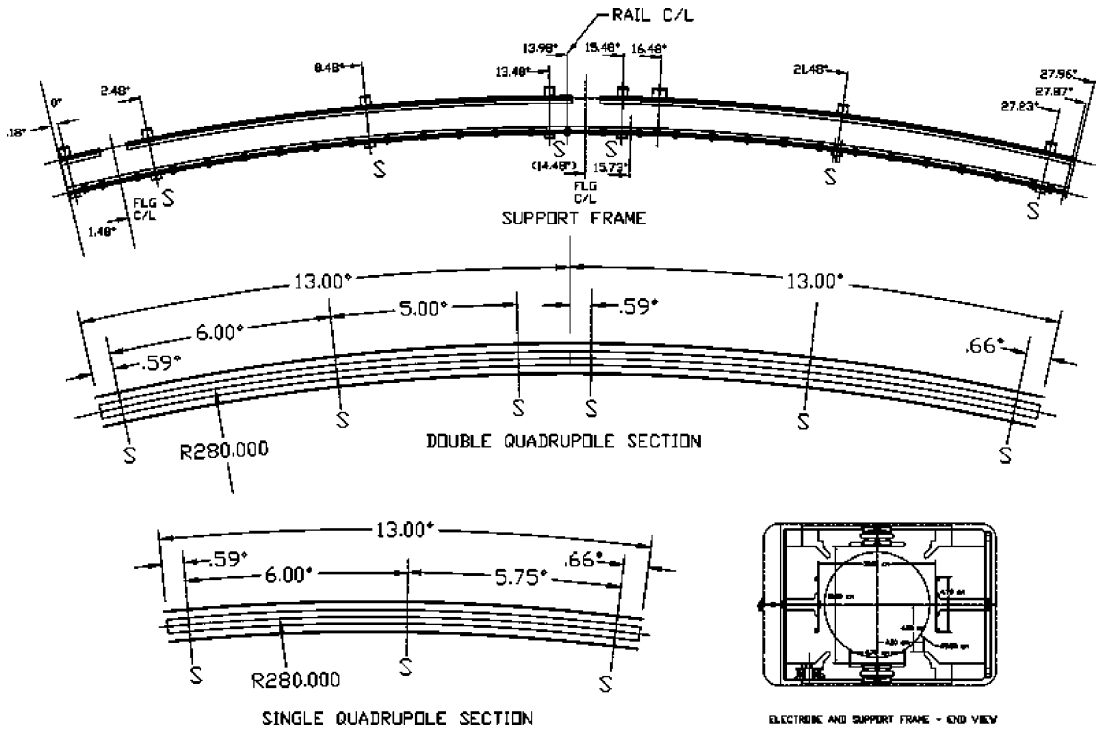

Fig. 9. The plan view of the electrode and support frame.

allow it to be "jacked" into vertical and radial alignment. The radial vacuum chamber ports give visual access to radial datum marks on the support frame for alignment using the theodolite system. A target on the bottom support frame plate is pulled through the chamber by a string for vertical alignment.

(4) The chambers are finally mounted into the gap of the storage ring magnet by positioning the chamber end flanges radially relative to the magnet pole inside radius. The less critical azimuthal (circumferential) position was determined by mounting features machined into chamber and the pole inside radial face.

(5) The ManCAT system was used to define the storage ring magnet geometry prior to the installation of experimental equipment. Eventually, the vacuum chamber dimensional database was folded into the global database of the storage ring. The overall goal of the quadrupole placement of ± 0.5 mm with respect to the ideal center of the ring at 7112 mm was confirmed by a special survey taken in July of 1998.

5. Trapping of atomic electrons

When the principle of the magic momentum was first applied to the CERN muon $(g-2)$ ring [3], it was found that it was not possible to apply a DC electric field necessary for the required field focusing index of $n = 0.139$, in the presence of the main magnetic field of 1.5T. After studying the behavior of the trapped electrons in the combined magnetic and electric fields, Flegel and Krienen [14] concluded that they could still do the experiment by applying a pulsed electric field of the order of 1ms, more than 15 stored muon lifetimes, with a reasonable pressure of $< 10^{-6}$ Torr.

Some of the conclusions from Ref. [14] are summarized here:

(1) Electron trapping occurs because free electrons get trapped by the combination of the E, B fields. The trapped electrons perform a combination of three motions while at the same time ionize the residual gas. This produces a charge avalanche and eventually a spark, discharging the quadrupole plates.
(2) The main source of free electrons is field emission from the high voltage quadrupole plates. Pion injection with 10^6 pions per bunch increased only slightly the electron trapping. To reduce the field emission they pulsed the quadrupoles with 20% higher voltage (a.k.a. conditioning) than the normal operating values for short times, e.g. 10 μs. This eliminated some whiskers and dust particles on the quadrupole plates and reduced field emission.

The stored (trapped) low energy electrons in a Penning trap perform a number of different motions shown in Fig. 10, a copy of Fig. 3 of Ref. [15], (see also Figs. 10 and 11 of Ref. [14]):

(1) Cyclotron motion due to the main dipole magnetic field. The angular frequency is [14] $\omega_B = eB/m_e \approx 2.7 \times 10^{11}$ cycles per s for the magnetic field of 1.5 T.
(2) Drift along the $\vec{E} \times \vec{B}$ direction (magnetron motion) with a velocity [14] of $(\vec{E} \times \vec{B})/B^2$.

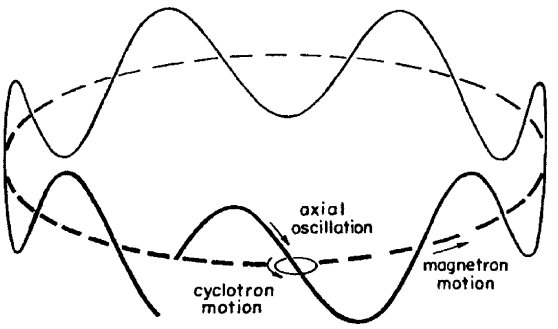

Fig. 10. A particle in a Penning trap performs a cyclotron motion, a magnetron motion and an axial oscillation. The low energy trapped electrons in the quadrupole regions of the $(g-2)$ ring perform similar motions.

(3) Vertical oscillation (axial oscillation) with a frequency of [14]

$$\omega_A = \left(\frac{eV}{m_e d^2}\right)^{1/2} = \left(\frac{ek}{m_e}\right)^{1/2} \quad (13)$$

where e is the electron charge, V is (approximately) the sum of the absolute values of the positive and negative voltages on the quadrupole plates. m_e is the electron mass, d the distance between the plates and k is defined as $E = -kx$, with x the radial coordinate.

We took advantage of the magnetron motion to quench the electron trapping and of the vertical oscillation to measure the electric field gradient as a function of voltage. The fact that we were able to quench the electron trapping allowed us to apply DC high voltage on the quad plates. This in turn allowed us to determine the resonance frequency of the trapped electrons and hence determine the electric field gradient as a function of the high voltage on the quadrupole plates. The DC high voltage also allowed us to set a sensitive limit on the influence of these trapped electrons on the E-field configuration and a limit on the generated B-fields due to the circulating charges.

5.1. Quenching of trapped electrons

In the negative muon storage polarity the volume of the electron trapping region is much larger than in the positive one [14]. In the following subsections we will be assuming that the quadrupoles are configured for negative muon storage, unless otherwise specified. The inferred limits apply to both polarities, being more stringent for the positive one. The drift velocity vector is given [14] by $(\vec{E} \times \vec{B})/B^2$. For $n = 0.137$ with 43% quad coverage of the $(g-2)$ ring, and a dipole magnetic field of $B = 1.45$ T, the drift velocity is equal to approximately

$$u = (7 \times 10^4 \text{ m/s}) \times x[\text{cm}] \quad (14)$$

where x is the radial distance from the center of the muon storage region in units of cm. The quadru-

pole electrode lengths of the short and long plates are approximately 1.6 and 3.2 m, correspondingly. When the trapped electrons reach the end of the plates the electric field shape is such that they re-enter the quadrupole region [14]. Therefore for a trapped electron 1 cm away from the center, it takes approximately 50 and 100 μs for the short and long plates, respectively, to travel the length of the quadrupole plates and return to the same point.

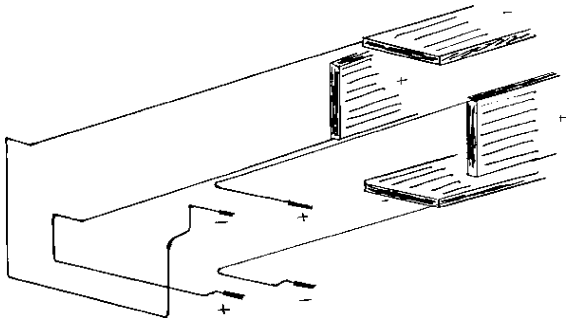

Fig. 11. A three dimensional representation of the quadrupole leads is shown in this schematic (not to scale). The lead geometry is such that the up/down, left/right symmetry is broken. The azimuthal extent of the leads is less than 10 cm.

The electron trapping occurs because the electrostatic quadrupoles combined with the vertical dipole B-field form a local penning trap for low energy particles. The fact that at the end of the quadrupole plates they return into the quadrupole region is due to the symmetry of the electric fields. We decided to break this symmetry at the one end of the plates by designing the quadrupole leads in a way that the quadrupole electric field is rotated by approximately 25° (see Figs. 8, 11, 12). The azimuthal extent of the leads is less than 10 cm

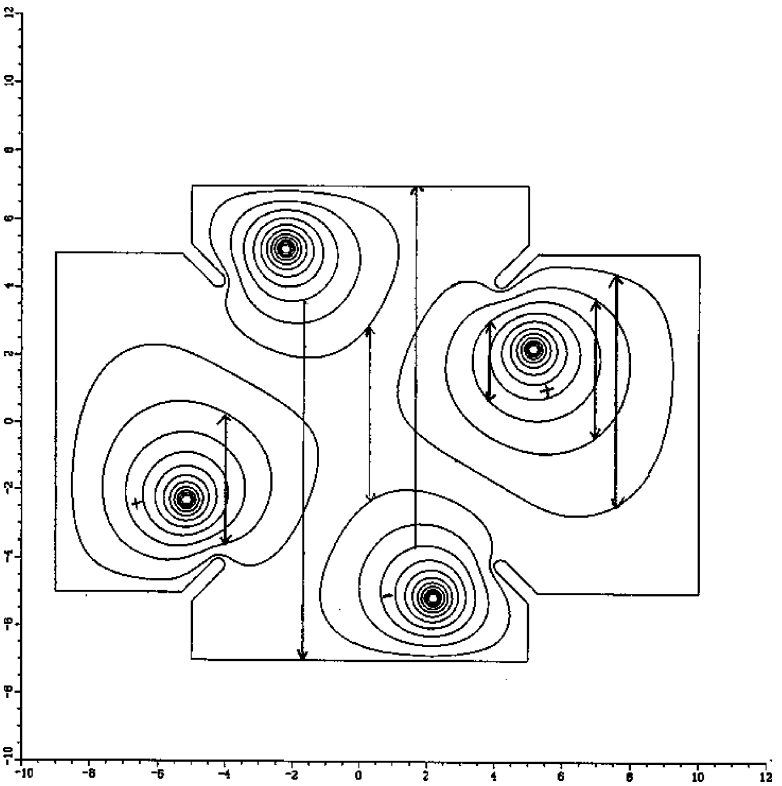

Fig. 12. The cross section of the leads, the trolley rails as well as the equipotential lines are shown. The vertical lines indicate the vertical motion of the trapped electrons at the lead location for the negative muon storage polarity. The trapped electrons that end up in the positive leads (left/right in this polarity) are eventually driven out to the feedthrough region due to the $\vec{E} \times \vec{B}$ drift. Most of the trapped electrons that end up in the central region are released while a small fraction remains captured. The units in the horizontal and vertical axes are in cm.

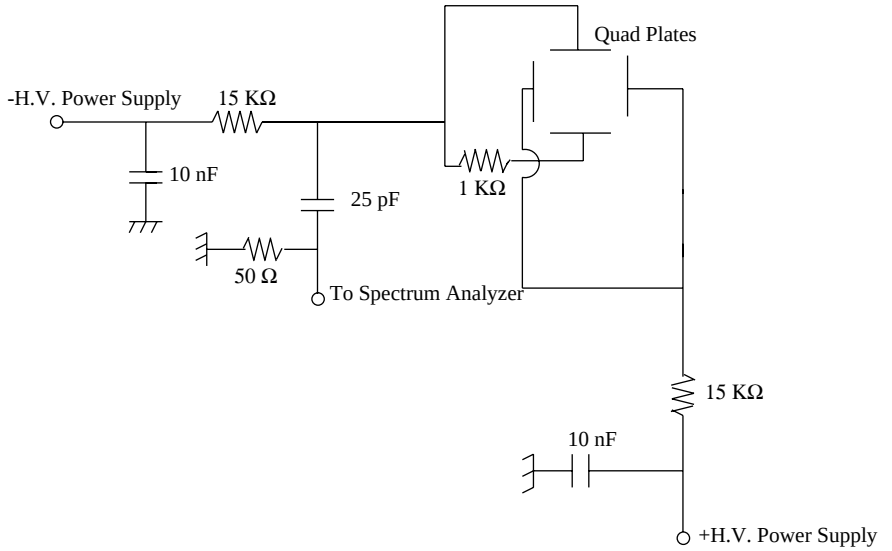

Fig. 13. The circuit used to observe the axial oscillation frequency of the trapped electrons as a function of the DC high voltage. The spectrum analyzer is decoupled from the DC high voltage by the 25 pF capacitor.

and does not contribute significantly to the multipoles of the average electric field. With this lead design we were able to apply much higher voltages on the plates in the pulsed mode and also to apply DC high voltage on the test module as follows: ± 14 kV for the negative muon storage polarity and ± 25 kV in the positive polarity. These values were achieved with the prototype quadrupole that had a length of 13°, or approximately 1.6 m while the pressure was better than 10^{-7} Torr. The electron trapping region is smaller in the positive polarity than in the negative and it is possible to apply a higher voltage on the plates.

The dominant effect for a spark to occur is the continuous accumulation of charge on the support insulators. In the negative muon storage polarity some of the trapped electrons, when they leave the region between the quadrupole plates, turn around [14] at the end of the quadrupole plates and travel on the outside of the vertical plates where they are intercepted by the support insulators. Eventually this accumulation of charge leads to a spark from the insulator to the positively charged vertical quadrupole plate. We found that we had to raise the voltage in the pulsed mode very slowly in order to be able to sustain the high voltage on the plates for hundreds of thousands of pulses without sparking.[1] The conditioning procedure for all the quadrupole plates at the same time took approximately 45 min to bring to full operating voltage.

5.2. Determination of the resonance frequency of the trapped electrons in the negative muon polarity

The trapped electrons in a quadrupole field behave like simple harmonic oscillators, i.e. their vertical oscillation frequency is independent of their amplitude when the top/bottom plates are negatively charged (for negative muon storage). Their frequency is given by Eq. (13) and can be used to determine directly the electric field strength as a function of voltage on the quadrupole plates.

We have used the circuit shown in Fig. 13 to observe this frequency in the DC high voltage mode. The motion of these electrons is incoherent and their image charge signal, on average, should

[1] During the $(g-2)$ experiment we were having a trolley run to measure the magnetic field every two to three days. We found that we had to condition the quadrupole plates each time after every trolley run. The maximum number of quadrupole pulses of roughly 1 million (corresponding to approximately three days) without a single spark, was recorded in the positive muon storage polarity. A more typical number was a few hundred thousand pulses between sparks, i.e. roughly one spark a day.

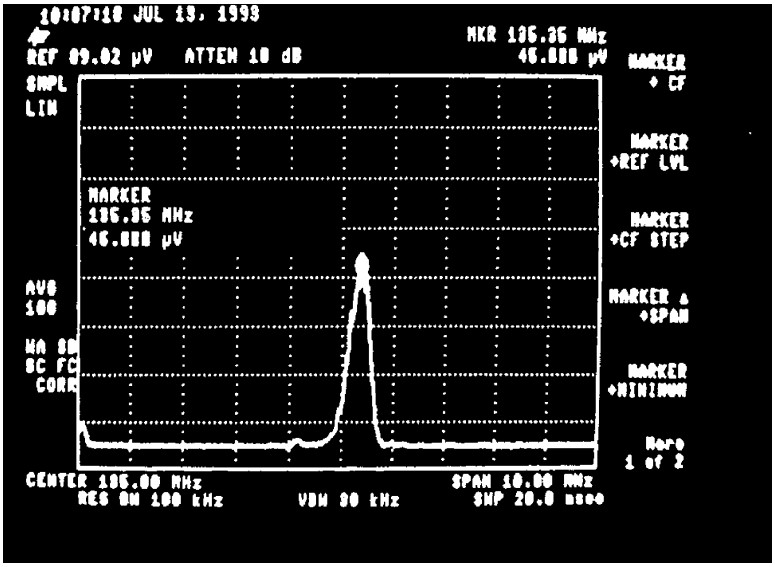

Fig. 14. A spectrum analyzer photograph of the resonance vertical oscillation frequency of the trapped electrons inside the quadrupole region. The resonance curve is the video average of 100 spectrum analyzer readouts. The voltages on the quad plates were +4.29 and −3.47 kV resulting in $\Delta V = 7.76$ kV. The frequency and the voltage at the peak are 135.35 MHz and 45.8 μV, respectively. The display resolution is 1 MHz per division.

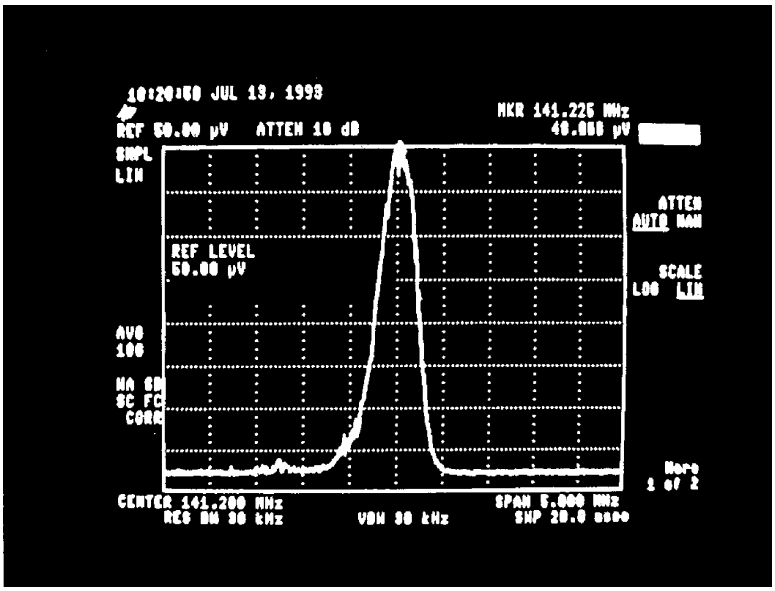

Fig. 15. A spectrum analyzer photograph of the resonance vertical oscillation frequency of the trapped electrons inside the quadrupole region. The resonance curve is the video average of 100 spectrum analyzer readouts. The voltage on the quad plates were +4.44 and −3.82 kV resulting to $\Delta V = 8.26$ kV. The frequency and the voltage at the peak are 141.225 MHz and 48.8 μV, respectively. The display resolution is 0.5 MHz per division.

be zero, but a small fluctuation in their numbers is enough to give a detectable signal on the spectrum analyzer. Figs. 14, 15 show the shape of this resonance at two different quadrupole voltages. The amplitude of the signal grows with higher voltage on the plates but the shape remains the same. Fig. 16 shows the frequency as a function of voltage. The points are the spectrum analyzer data and the line is the expected frequency assuming a pure quadrupole field.

5.3. Influence of the trapped electron charge buildup to electric and magnetic fields

In order to determine the electric field correction on the anomalous magnetic moment we need to know the electric field gradient to 5% [16]. For beam dynamics reasons we require the electric field to be stable to $\pm 0.5\%$ whereas we need to know the magnetic field to 0.1 ppm. Therefore the electric field we create with the quadrupoles needs to be stable to $\pm 0.5\%$, the produced trapped electrons must not alter the electric field gradient to the same level, and must not create magnetic fields more than 0.1 ppm.

Since the application of the DC high voltage showed no deviation of the electron resonance frequency from the expected values, a very strict limit on the change of the electric field in the quadrupole region is possible. Most of the trapping for negative polarity muon storage occurs in the center of the storage region where there is a low $(\vec{E}\times\vec{B})/B^2$ drift velocity of the trapped electrons. The observed signal comes from the low energy trapped electrons and therefore it provides a direct indication of the electric field influence at the location of interest.

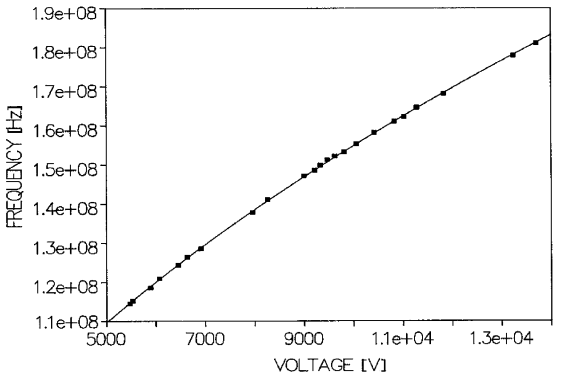

Fig. 16. The resonance frequency versus $\Delta V \equiv |V^+| + |V^-|$ the DC high voltage applied to the quadrupole plates. The line is the fit to the data assuming a perfect quadrupole field versus voltage.

The signal amplitude had a maximum of about 100 μV which for 50 Ω termination impedance corresponds to $I = V/R \approx 2\ \mu A$. The induced current is due to the oscillating charges with the resonant frequency:

$$I = \frac{dQ}{dt} = \omega_{h.o.}\ Q_0 \sin(\omega_{h.o.} t) \tag{15}$$

which for $\omega_{h.o.} = 2\pi \times 153$ MHz corresponds to $Q_0 \approx 2 \times 10^{-15}$ C or about 13,000 electrons. Since the electrons are moving with random phases it is expected that on average the signal should be zero. However, the fluctuations in the number of electrons with opposite phases allow for a non-zero signal amplitude. Assuming these fluctuations to be purely of statistical origin, we estimate the total number of trapped electrons to be equal to $(13{,}000)^2 = 1.7 \times 10^8$. The capacitance of the short top and bottom plates is ≈150 pF which means for a voltage of 10 kV the stored charge is $Q = CV = 1.5 \times 10^{-6}$ C or approximately 10^{13} charges thus the estimated number of trapped electrons is only ≈20 ppm of the total number of charges stored in the plates. Since most of the trapped electrons are created due to ionization of the residual gas present in the vacuum chamber, there is approximately one positively charged ion present in the quadrupole region for every trapped electron. Positively charged particles of course are not confined vertically by the electrostatic quadrupoles, configured for vertical focusing of negatively charged particles, and therefore the ions end up either on the bottom or the top plate. These positive ions will deplete the charge from the quadrupole plates at the very small level of ≈20 ppm.

From Eq. (13) we have that the axial frequency is proportional to $\sqrt{k}$ with k defined as $E = -kx$. Therefore by observing the trapped electron axial frequency we are probing directly the electric field gradient inside the quadrupoles. Most of the trapped electrons are located in the central region and if they altered the electric field in that location

by a substantial amount it would appear as a shift in the axial frequency. The width of the detected signals in Figs. 14, 15 is 0.5 MHz, i.e. $\Delta f/f < 0.4\%$ and since the peak frequency is consistent with the expected value using Eq. (13), see Fig. 16, it sets a limit of $\Delta k/k < 0.8\%$. Since in the DC high-voltage mode the charge accumulation inside the quadrupole region is many orders of magnitude greater than in the pulsed mode, we can safely conclude that the presence of the trapped electrons alters the E-field in that location much less than the beam dynamics requirement of $\pm 0.5\%$.

5.4. Limit on B-field generation due to the trapped electron current

The circulating low energy trapped electrons are a source of a magnetic field. This magnetic field source is not present when the NMR beam-tube trolley measures the storage ring magnetic field since the quadrupoles are turned off during that period. It is therefore important to determine the level of that B-field. It turns out that the voltage stability requirement of $\pm 0.5\%$ throughout the pulsed quadrupole voltage already places an adequate limit.

It is important that the electron trapping is a slow effect and it takes hundreds of μs to develop [14]. The high voltage storage capacitors (see next section) of 1.5 μF are connected to the distribution cables and through them to the quad plates only during the thyratron switch-on time. The total capacitance of the distribution cables that feed the top plates is $C = 3$ nF, and similarly for the bottom plates.

Most of the trapped electrons are generated in the middle of the quadrupole region where their speed is very small. For a typical duration of 1 ms long pulses only a very small region, i.e. 0.5–1 mm from the center creates trapped electrons which drift slow enough that they may not make it even once around the quadrupole length and therefore they will be free to ionize the residual gas during the whole pulse duration. In this region for every ionized residual gas there is a positive ion generated that ends up either on the top or bottom electrode and depletes its charge.

After the Thyratron switches are turned off (see next section) the dominant capacitor still connected to the quadrupole plates is the distribution cables. As was mentioned above the top quadrupole plates are connected to distribution cables with a total capacitance of $C = 3$ nF and the same is true for the bottom plates. A $\pm 0.5\%$ voltage stability requirement means that the maximum voltage drainage that can occur during a 25 kV quadrupole powering is equal to $\mathrm{d}V = 250$ V or a total charge drainage of $\mathrm{d}Q = C\,\mathrm{d}V = 0.75$ μC from the sum of all the top plates. The maximum charge that is generated can be twice that when taking into account the bottom plates as well, i.e. $\mathrm{d}Q = 1.5$ μC. This limit is very conservative since a large fraction of the trapped electrons are taken out of the muon storage region by the special design of the quadrupole leads which does not affect the ions. Making the reasonable assumption that the charge depletion around the ring is proportional to the azimuthal coverage of the quadrupole plates, the total charge available per short quad section is 12 times smaller, i.e. $\mathrm{d}Q = 0.125$ μC.

Assuming the circulating electrons are restricted vertically along an infinitely long plane and are drifting azimuthally due to the $\vec{E} \times \vec{B}$ fields, then the magnetic field generated by the circulating electrons is equal to

$$B = \mu \frac{K}{2} = \mu \frac{\mathrm{d}Q}{\mathrm{d}t\, y_0\, 2} \tag{16}$$

with $\mathrm{d}t$, taking into account Eq. (14), equal to

$$\mathrm{d}t = \frac{2 l_s}{7 \times 10^4\ \mathrm{m/s} \times x[\mathrm{cm}]} \tag{17}$$

which is, at minimum, equal to $\mathrm{d}t = 7.5$ μs for $x = 5$ cm, and $l_s = 1.6$ m the azimuthal length of the short quad units. K is the current density of the current sheet and $y_0 \approx 10$ cm is its height. Then, the maximum, locally generated B-field can be equal to

$$B = 4\pi 10^{-7} \frac{\mathrm{Vs}}{\mathrm{Am}} \frac{0.125\ \mu\mathrm{C}}{2 \times 7.5\ \mu\mathrm{s} \times 0.1\ \mathrm{m}} \approx 0.1\ \mu\mathrm{T}. \tag{18}$$

It turns out the limit of the B-field inside the long quads is also 0.1 μT. Taking into account that the quadrupoles only cover 43% of the total storage ring circumference and the fact that the main dipole field is equal to 1.45 T, the integrated maximum B-field disturbance is equal to 0.03 ppm. In reality the limit on the field is much better, since 1% of the stored charge would lead to frequent high voltage breakdowns.

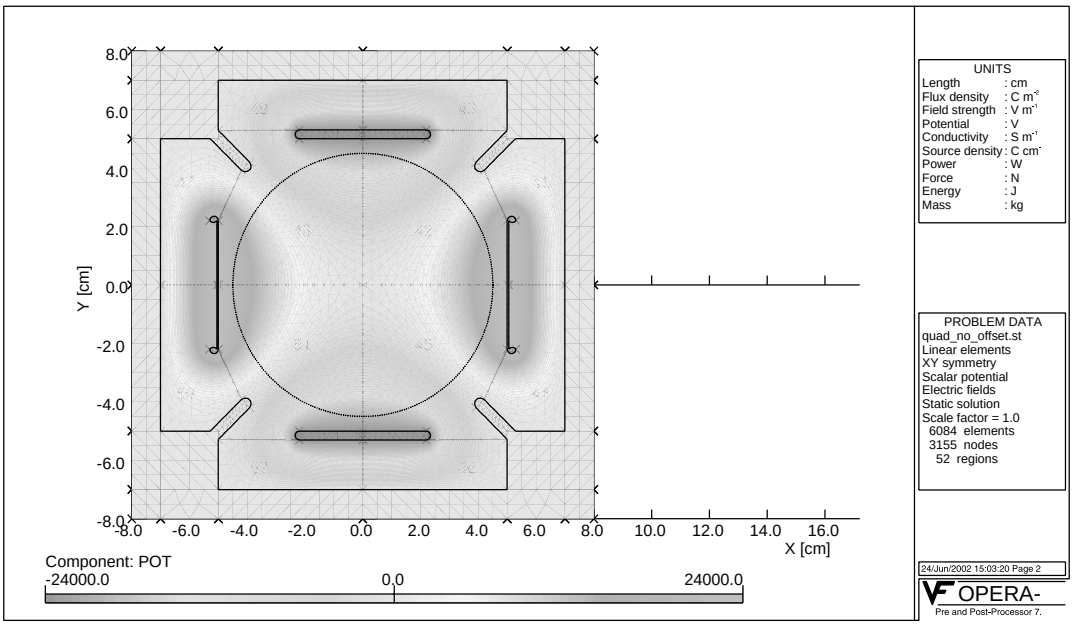

Fig. 17. The quadrupole plates and the equipotential regions for ± 24 kV on the plates. The dotted circle has a diameter of 9 cm and denotes the cross section of the muon storage region. The placement of the quadrupole plates was assumed to be ideal.

It is therefore not surprising that when we looked for an extra magnetic field with the quads turned on at ± 10 kV and off every other ≈ 50 s we did not observe any signal. The NMR probe was located on top of the vacuum chamber, and its relative signal sensitivity was 10^{-8}. In the almost DC mode (more than 50×10^3 times longer compared to ≈ 1 ms during data taking) the accumulated charge is far larger than in the pulsed mode. This is so even though the high voltage value of 10 kV is smaller by about a factor of 2.5 compared to that applied in the pulsed mode.

6. Multipoles of the electrostatic potential in the quadrupole region

6.1. Multipoles at normal operating voltage

The potential inside the electrostatic quadrupole region can be, to a good accuracy,[2] expressed as the sum of multipoles:

$$U = \sum_{n=0}^{\infty} r^n [a_n \sin(n\vartheta) + b_n \cos(n\vartheta)] \tag{19}$$

where $x = r\cos\vartheta$ and $y = r\sin\vartheta$ are the horizontal (radial) and vertical coordinates respectively. The multipole analysis is done with OPERA [17] and Fig. 17 shows the equipotential regions for ± 24 kV on the quad plates. The width of the electrode can be adjusted to make b_6 equal to zero. When this is done, $b_{10}/b_2 = 1.9\%$ at the edge of the circular aperture. The potential inside the storage region minus the quadrupole field[3] is shown in Fig. 18.

In Table 5 we show the potential multipoles when the quad plates are charged with ± 24 kV for negative muon storage polarity. The placement of the plates is assumed ideal. In Table 6 we show the potential multipoles when the quad plates are charged with ± 24 kV for negative muon storage polarity and the placement of the plates is assumed the worst possible, i.e. ± 0.75 mm on the side plates, and ± 0.5 mm on the top/bottom ones. To

[2] Under the assumption that the quadrupole plates are straight and not curved, this expression is exact. The curvature effects were investigated, but are not discussed here.

[3] In order to make more visible the dominant multipoles.

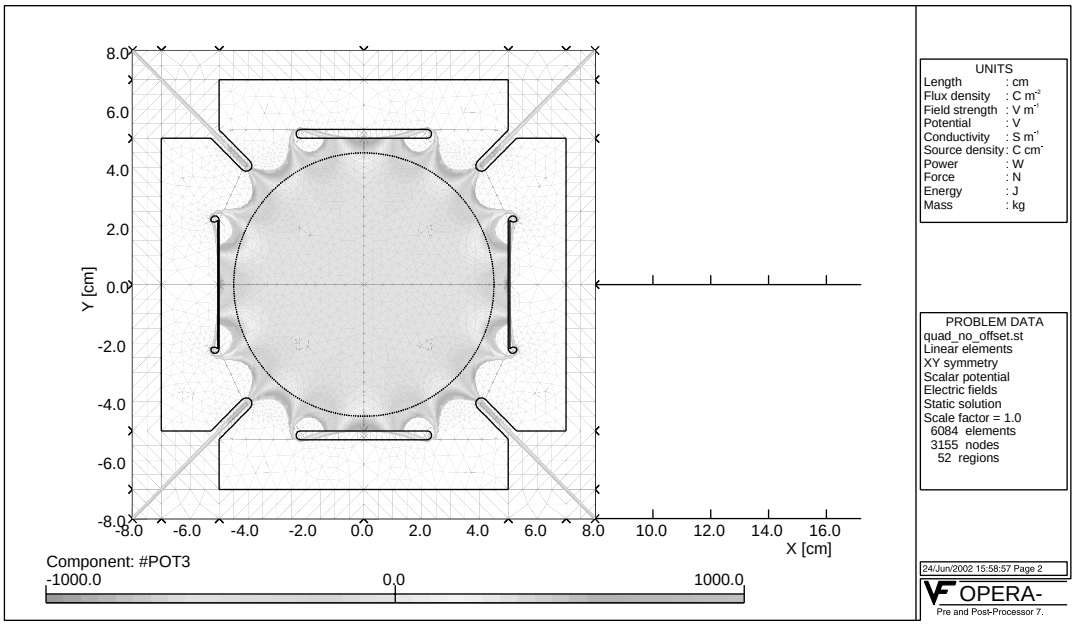

Fig. 18. The plotted parameter #POT3 is the regular potential (plotted in Fig. 17) minus the quadrupole potential and is defined as $\#\mathrm{POT3} = \mathrm{POT} - (\mathrm{POT}_{2\,\mathrm{cm}}/2^2)*(x^2 - y^2)$. The dominance of the 20 pole, $b_{10}/b_2 = 1.9\%$ on the circle with $r = 4.5$ cm, is clearly visible.

Table 5
The potential multipoles at $r = 4.5$ cm, the edge of the muon storage region, for negative muon storage and ± 24 kV on the plates

Order of multipole	Cosine term (Normal) [V]	Sine term (skewed) [V]
1	0.0 (−12)	0.0
2	20177.8	0.1
3	0.0 (−28)	0.0
4	33.0 (−153)	0.1
5	0.0 (−10)	0.0 (−8)
6	−45.9 (−26)	0.1
7	0.0	0.0
8	−5.5	−0.2
9	0.0	0.0
10	−391.3	0.1
11	0.0	0.0
12	−6.5 (18)	0.0
13	0.0	0.0
14	52.3	−0.1

The placement of the plates is assumed ideal and the distance of the plates from the vacuum chamber walls is equal for all plates as shown in Fig. 17. In parentheses we show the multipoles generated due to the scalloped vacuum chambers violating the four fold symmetry.

Table 6
The potential multipoles at $r = 4.5$ cm, the edge of the muon storage region, for negative muon storage and ± 24 kV on the plates

Order of multipole	Cosine term (normal) [V]	Sine term (skewed) [V]
1	405	345
2	19875	−75
3	173	−120
4	−190	20
5	−10	−8
6	−35	30
7	−50	35
8	20	10
9	−50	−30
10	−391.3	0
11	−15	10
12	20	4
13	4	2
14	50	−2

The placement of the plates is assumed to be the worst possible (i.e. ± 0.75 mm on the side plates, and ± 0.5 mm on the top ones). The multipoles shown are the highest values found when different combinations of non ideal quad plate positioning is assumed.

Table 7
The potential multipoles at $r = 4.5$ cm, the edge of the muon storage region, for negative muon storage and ± 24 kV on the plates except on the bottom plate of -17 kV. The placement of the plates is assumed ideal

Order of multipole	Cosine term (normal) [V]	Sine term (skewed) [V]
1	0	−2155
2	18706	0
3	0	837
4	375	0
5	0	−117
6	−41	0
7	0	−57.5
8	−76	0
9	0	52
10	−364	0
11	0	−8
12	−3	0
13	0	−5
14	49	0

Table 8
The potential multipoles at $r = 4.5$ cm, the edge of the muon storage region, for negative muon storage and -24 kV on the top, $+24$ kV on one side, -17 kV on the bottom and $+17$ kV on the other side electrode. The placement of the plates is assumed ideal

Order of multipole	Cosine term (normal) [V]	Sine term (skewed) [V]
1	−2150	−2156
2	17235	0
3	−840	837
4	28	0
5	−121	−117
6	−39	0
7	−57	−57
8	−5	0
9	53	52
10	−334	0
11	9	−8
12	−6	0
13	−5	−5
14	45	0

produce this table we used the maximum generated multipole amplitude under different combination of quad plate misplacement.

6.2. Multipoles during scraping

In Table 7 we show the potential multipoles under vertical scraping,[4] i.e. when the quad plates are charged with ± 24 kV for negative muon storage polarity, except the bottom plate is charged with -17 kV. The placement of the plates is assumed ideal. In Table 8 we show the potential multipoles when the quadrupole plates are charged with -24 kV on the top, $+24$ kV on one side, -17 kV on the bottom and $+17$ kV on the other side electrode. The placement of the quad plates is assumed again ideal.

The amplitude of the multipoles track quite well with the difference between the maximum and minimum voltage on the plates in a particular quad section. This simplifies the estimation of the multipoles at different scraping voltages.

[4] Horizontal and vertical scraping is used to eliminate the beam halo in order to reduce muon losses during the storage time [1].

7. HV pulser and scraping

7.1. Electrical circuits

The electrical diagram of the quadrupoles is given in Fig. 19. The storage capacitance is 1.5 μF, rated at 40 kV [18]. The high voltage (HV) switches are deuterium thyratrons, models CX1585A and CX1591, made by EEV [19], rated at the minimum to 40 kV, and 5 kA. The power supplies which were capable of delivering 30 kV at 10 mA maximum, were models PS/ER30P10.0Y65 for the positive and PS/ER30N10.0Y65 for the negative high voltage from Glassman [20]. Their voltage regulation is $<0.005\%$ whereas their ripple: $<0.02\%$ RMS of rated voltage $+0.5$ V at full load.

The capacitance of the distribution cables (RG35B) is between 1 and 3 nF depending on how many quadrupole plates are fed, deployed in the star configuration, by the same HV pulser unit. There are four pulser units, two for applying standard high voltage (i.e. a single voltage value per pulse), one for each polarity, and two for scraping high voltage (i.e. two different voltage values per pulse), again one for each polarity.

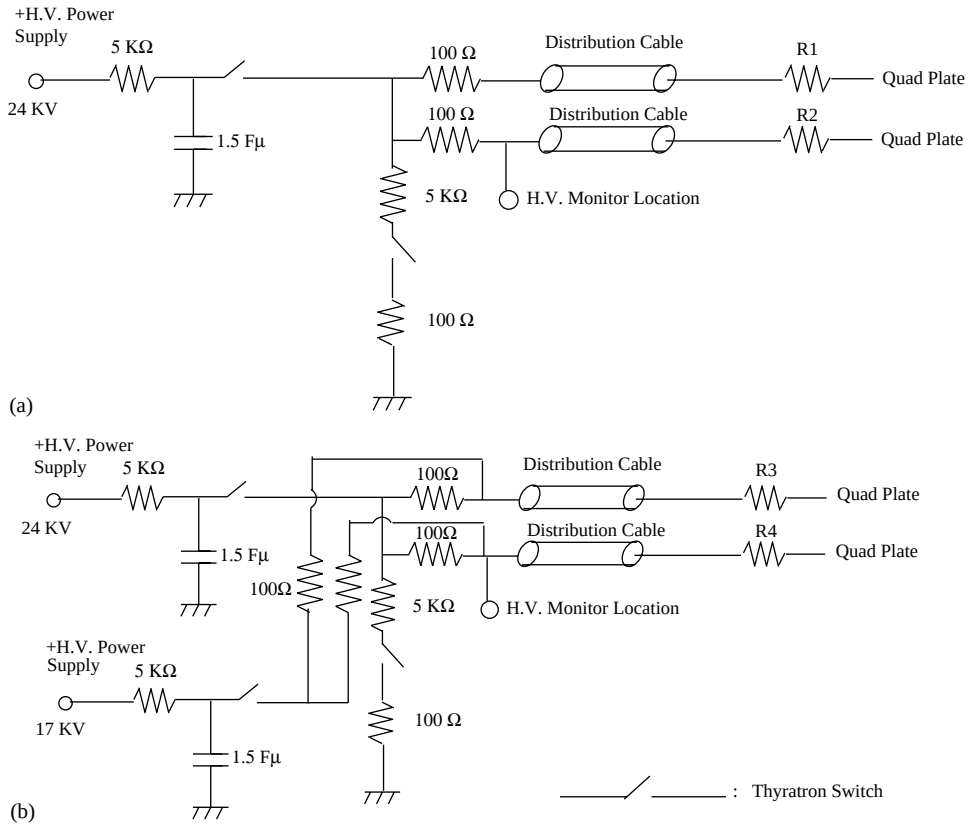

Fig. 19. The electrical circuit for (a) positive standard high voltage of 24 kV and (b) for positive high voltage of 24 kV with scraping of 7 kV on the quadrupole plates. There are two more units similar to these connected to negative high voltage power supplies. The switch connected to the standard high voltage circuit and the one connected to the lower high voltage power supply on the scraping high voltage circuit, were turned on 30–50 μs before beam injection. The switch connected with the higher voltage power supply was turned on 16 μs after beam injection for the runs of 1997–2000 and 7 μs after beam injection for most of the run of 2001. All the quadrupole plates were discharged approximately 1 ms after injection.

Typical waveforms of the positive, standard and scraping, and the corresponding for negative high voltage is shown in Fig. 20. The pulser units are shown in Fig. 21, the four tall units positioned in the middle of the ring with one unit being worked on. The capacitance of the quad plates is given in Table 9. The values of the resistors attached to them, located between the distribution cables and the quad leads, are also given for each plate. The capacitance value of each quad plate was checked at the beginning of each run to ensure continuity and plate position stability. The thyratron switches are triggered by an external pulse of 800 V and stop contacting when the current flowing is below 500 μA. A typical cycle included a burst of 12 pulses 33 ms apart while the overall accelerator cycle was between 2.7 and 3.2 s.

7.2. Parameters during quadrupole scraping

The scraping creates a gap between the muon beam and the collimators defining the diameter, $2r = 9$ cm, of the circular aperture. The scraping time was set to be 16 μs for the runs of 1997, 1998, 1999 and 2000. The scraping time for the year 2001 was set to be only 7 μs. The scraping voltage varied, but most of the data were taken with 7 kV. The scraping configuration for an operating voltage of ≈ 24 kV and $n \approx 0.137$, is given in Table 10. All the top plates and all the side plates of Q_1

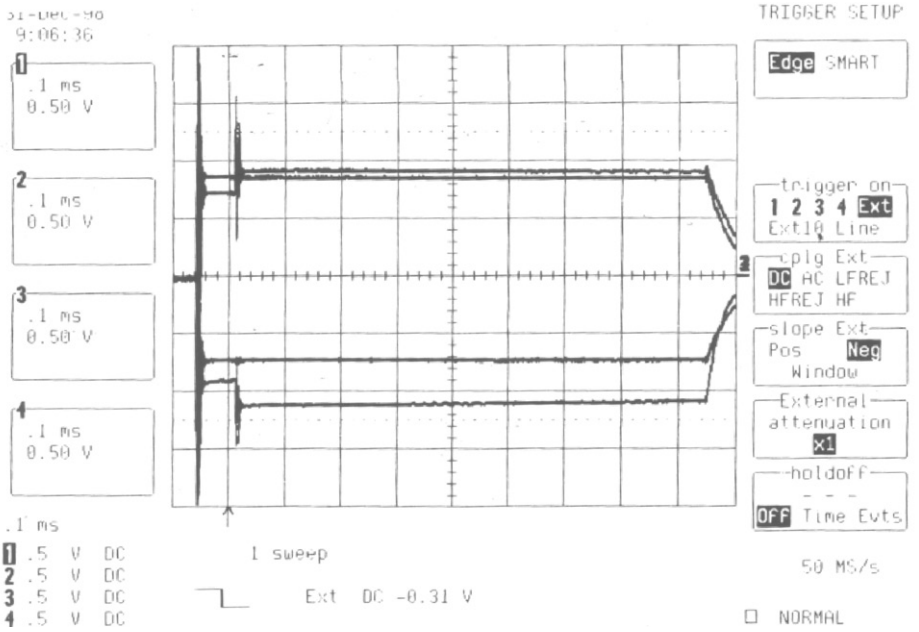

Fig. 20. An oscilloscope display (with a scale of 100 μs/div in the horizontal and 0.5 V/div in the vertical) of four quadrupole waveforms, two positive and two negative, are shown; the output of home made high voltage monitors connected to the circuit points indicated in Fig. 19. The arrow (trigger point) denotes the muon injection time; scraping ends 16 μs later (see text) with a rise time of ≈ 5 μs. The high voltage values at injection are ± 24 kV for the standard ones for both polarities. For the scraping ones the high voltage at injection is ± 17 kV (for 7 kV scraping) before they reach full voltage of ± 24 kV. The difference in their calibration coefficients is quite large as evident by their displayed amplitude. The spikes are due to their limited frequency compensation.

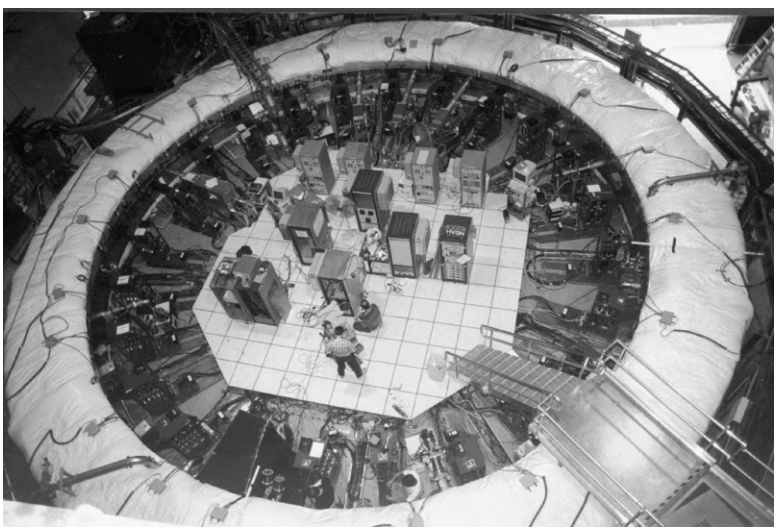

Fig. 21. A photograph from above of the muon ($g-2$) storage ring. The four quadrupole pulser units are located in the middle of the ring, with one unit being worked on.

Table 9
Quadrupole plate plus high voltage monitor total capacitance (top [pF]) and resistor (bottom [KΩ]) used. The plates with high voltage monitors attached to them permanently are shown in bold

Quad section	Top plates	Bottom plates	Inner plates	Outer plates
Q_1 short	129	136	78	87
	36	36	72	72
Q_1 long	250	252	144	152
	20	20	36	36
Q_2 short	132	139	**216**	88
	36	36	20	72
Q_2 long	249	256	140	148
	20	20	36	36
Q_3 short	133	145	80	88
	36	36	72	72
Q_3 long	248	**416**	141	150
	20	12	36	36
Q_4 short	137	136	79	**230**
	36	36	72	20
Q_4 long	252	251	146	**292**
	20	20	36	20

Table 10
Quadrupole plate voltage [kV] at injection time for the negative muon storage polarity

Quad section	Top plates	Bottom plates	Inner plates	Outer plates
Q_1	−24	−17	+24	+24
Q_2	−24	−17	+17	+24
Q_3	−24	−17	+24	+24
Q_4	−24	−17	+24	+17

and Q_3 were charged to their final voltage of 24 kV already at injection time. The same was true for the outer plates of Q_2 and the inner plates of Q_4. All the bottom plates were charged to 17 kV at injection time, the same as the inner plates of Q_2 and the outer plates of Q_4. After scraping time the scraping plates were all brought up to full voltage of 24 kV with a rise time constant of 4.5–5 μs depending on the plate.

The vertical and horizontal beam motions during and after scraping were quantitatively investigated by particle tracking simulations, using the two-dimensional map of the actual electric field determined with OPERA [17]. Experimentally, the focusing field index, n, defined in the "smoothed" approximation (see Section 2), was observed during scraping by scintillation fiber monitors. The n-value after scraping was well determined from the Fourier analysis of the decay electron spectrum. Here we represent only the basic ideas of the beam scraping in this experiment.

As follows from Eq. (19), the electric potential

$$\begin{aligned} U = {} & b_1 x + a_1 y + b_2(x^2 - y^2) + 2a_2 xy \\ & + b_3(x^3 - 3xy^2) + a_3(3x^2 y - y^3) \\ & + b_4(x^4 - 6x^2 y^2 + y^4) \\ & + 4a_4(x^3 y - xy^3) + \cdots \end{aligned} \tag{20}$$

and hence the electric fields

$$\begin{aligned} E_x = {} & -b_1 - 2b_2 x - 2a_2 y - 3b_3(x^2 - y^2) - 6a_3 xy \\ & - 4b_4(x^3 - 3xy^2) - 4a_4(3x^2 y - y^3)\ldots \end{aligned} \tag{21}$$

$$\begin{aligned} E_y = {} & -a_1 + 2b_2 y - 2a_2 x + 6b_3 xy - 3a_3(x^2 - y^2) \\ & + 4b_4(3x^2 y - y^3) - 4a_4(x^3 - 3xy^2)\ldots\ . \end{aligned} \tag{22}$$

Let us consider first pure vertical scraping, assuming a zero horizontal magnetic field. Let the voltage on the upper electrodes, as well as the electrodes on sides, equal V_0, and the voltage on the bottom electrodes V_1. The corresponding electric potential for $V_0 = 24$ kV and $V_1 = 17$ kV is given in Table 7, and we must compare it with Table 5, where $V_1 = V_0 = 24$ kV. During pure vertical scraping, the fields in all four quadrupoles are the same. Since there are no vertical forces in space between quadrupoles, we can get the ratio of the perturbed average ("smoothed") field index n_1 to the unperturbed average n as the ratio of the b_2-coefficients in Tables 7 and 5:

$$\frac{n_1}{n} = \frac{18706}{20178} = 0.927; \quad \frac{\Delta n}{n} \equiv \frac{n_1 - n}{n} = -0.073 \approx -\frac{V_0 - V_1}{4V_0} \tag{23}$$

for only vertical (without horizontal) scarping. Further, we have the shift of the vertical equilibrium position (i.e., the position where $E_y = 0$) from $y = 0$ down toward the lower voltage:

$$\Delta y = 45\frac{a_1}{2b_2}\,\text{mm} = -2.59\ \text{mm} \approx -0.79\frac{V_0 - V_1}{4V_0} \times 45\ \text{mm} \quad (24)$$

for only vertical scraping. After scraping, the parameters go to their normal values, $V_1 \to V_0$, $n_1 \to n$, and $\Delta y \to 0$, but now there is a 2.6 mm gap between the collimators and the vertical spread of the beam. This is the idea of the vertical scraping. With respect to this idea, one question is whether the produced gap survives betatron resonances (see Figs. 3 and 4) crossed by muons while the field focusing index goes from n_1 to n. To answer this question quantitatively, we analyze the muons having maximal betatron amplitudes, $x^2 + y^2 \approx r^2$, $r = 45$ mm, taking into account field perturbations. The betatron oscillations of such muons are non-linear, and the best way for such analysis is tracking simulations. A brief discussion of the resonance crossings will be given below for the realistic case of both vertical and horizontal scraping.

There is an essential difference between horizontal and vertical scrapings. The distortion of the vertical closed orbit can be considered as the result of the resonance at $\nu_y = 0$. For horizontal scraping, it is practically impossible to use this method of vertical scraping in which all quadrupoles have the same scraping voltages. The reason is that the radial orbit is strongly stabilized by the magnetic field, so $\nu_x^2 = (1 - n) \gg \nu_y^2 = n$, and in order to shift the orbit horizontally by the same method and at the same distance as we do vertically, we need the perturbation $\Delta V_x \approx (1 - n)\Delta V_y/n \approx 6.3\Delta V_y$. In horizontal scraping, we use a different resonance perturbation based on the fact that the horizontal frequency operation values, (see Fig. 3 and Table 3), $\nu_x = 0.938, 0.930, 0.927$, are close to the resonance $\nu = 1$. (Note that the use of non-zero modes of resonance perturbations for vertical scraping is practically impossible, since the operating values $\nu_y \approx 0.351, 0.372$, and 0.379 are far from the resonances at $\nu = 1, 2, \ldots$) In our procedure, according to Table 10, the signs of b_1 (as well as b_3), see Eqs. (21) and (22), are different for Q_2 and Q_4. This alternating perturbation of the inner and outer plates produces a horizontal resonance harmonics,

$$E_x = 0.42 b_1 \cos\theta + \cdots \quad (25)$$

which enters into the equation of the muon horizontal oscillations:

$$\frac{d^2x}{d\theta^2} + (1 - \langle n_2 \rangle)x \approx 0.94\langle n_2 \rangle \frac{b_1}{2b_2}\cos\theta + \cdots \quad (26)$$

Here x is expressed in r-units, $r = 45$ mm, and $\langle n_2 \rangle$ is the average ("smoothed") field index in this case of simultaneous vertical and horizontal scraping when the Q_2 and Q_4 quadrupoles have a smaller local n-value than quadrupoles Q_1 and Q_3.

$$\frac{\langle n_2 \rangle - n}{n} = \frac{(17235 + 18706) - 2 \times 20178}{2 \times 21078} = -0.11 \approx -1.5\frac{V_0 - V_1}{4V_0}. \quad (27)$$

The local horizontal shift of the points where $E_x = 0$,

$$\frac{\Delta x(mm)}{45} = \frac{b_1}{2b_2} = \frac{2150}{2 \times 17235} = 0.062 \approx 0.85\frac{V_0 - V_1}{4V_0} \quad (28)$$

is positive at Q_4 and negative in Q_2. (It is absent in Q_1 and Q_3.) In (25), we choose $\theta = 0$ in the center of Q4. The perturbations $E_x = (\partial E_x/\partial x)_0 \Delta x \sim n\Delta x$ in Q_4 and Q_2 are proportional to the *local*, not average, field index (if Δx is given). It is for this reason that factor 0.42 of Eq. (25) almost disappears in Eq. (26) when we put $\langle n_2 \rangle$ there instead of $n_{\text{local}} \sim \langle n_2 \rangle / 0.43$. Higher modes in Eqs. (25) and (26) can be neglected since their influence on x is $8/n \sim 50$ times weaker than the influence of the main mode, $\cos\theta$, even if all amplitudes are equal. From Eq. (26), the perturbed equilibrium

$$x_{\text{eq}} \approx X\cos\theta, \quad X \approx 36\frac{V_0 - V_1}{4V_0}\,\text{mm} = 2.6\ \text{mm}. \quad (29)$$

In the following Eqs. (29) to (34), the numerical results correspond to parameters of Table 10. The

value of X and the simple sinusoidal behavior of x_{eq}, with no visible 3rd mode, were confirmed by simulations. In these simulations, we saw beating between the equilibrium orbit (Eq. (29), $x_{eq}(\theta)$, $\theta = 2\pi ft$, where f is the revolution frequency), and the free betatron oscillations *around this equilibrium orbit*. This gives us a 2.6 mm horizontal gap after scraping, when $X \to 0$.

As for the vertical part of the x, y simultaneous scraping, it can be seen from Tables 7 and 8 that the vertical shift, almost constant around the ring, equals

$$\Delta y = -Y, \quad Y \approx 37 \frac{V_0 - V_1}{4V_0}\,\text{mm} \approx 2.7\ \text{mm} \qquad (30)$$

which gives 2.7 mm vertical gap after scraping.

The final gap between the muon beam and collimators depends not only on X and Y, but also on beam behavior on the edge. First, the vertical oscillations get an additional gap, ΔY, during the adiabatic transition $\langle n_2 \rangle \to n$. This gap depends on the maximal possible y-amplitude, which depends on the $\sin \vartheta$:

$$\Delta Y_{ad} = \frac{1}{4}\left|\frac{\Delta n}{n}\sin\vartheta\right| \times 45\ \text{mm} = 1.2|\sin\vartheta|\ \text{mm}. \qquad (31)$$

The angle ϑ is defined in Eq. (19). In horizontal oscillations, such adiabatic effect is practically absent; instead, the horizontal gap is increased by a half-integer parametric resonance caused by the 2nd harmonics of the local $n = n(\theta)$ present during scraping, $(n(\theta) - \langle n_2 \rangle) \propto \cos 2\theta$. As a result

$$\Delta X_{par} \approx 1.5|\cos\vartheta|\ \text{mm}. \qquad (32)$$

Second, both oscillations get additional ΔX_3, ΔY_3 due to the appearance of the cubic term in the potential, $a_3 \approx -b_3 \approx 840$ in Table 8, see terms $(x^2 - y^2)$ in Eqs. (21) and (22). Since $x_{max}^2 - y_{max}^2 = \cos 2\vartheta$ (in r-units, $r = 45$ mm),

$$\Delta X_3/X \approx 1.5\frac{b_3}{b_1}\cos 2\vartheta \approx 0.6\cos 2\vartheta \qquad (33)$$

$$\Delta Y_3/Y \approx 1.5\frac{a_3}{a_1}\cos 2\vartheta \approx -0.6\cos 2\vartheta. \qquad (34)$$

Thus, the total gap between the beam and the collimators after scraping depends on ϑ. It is partly reduced by the muon momentum spread and by an undesired horizontal magnetic field, as well as by resonances crossed during transition to the normal operating values. As for resonance crossings, we see from Fig. 3 and Eq. (27) that, during the operation at value $n = 0.142$, muons do not cross the resonance at 0.126; during the operation at value 0.137, they do; and during the operation at value 0.122, they cross a rather weak resonance at 0.111 when returning to the designed parameters after scraping. (There are also other resonances which we will not discuss here.) The two resonances mentioned above disappear at small y's, so the gaps for oscillations close to the horizontal plane survive these particular crossings. Whatever the changes of the beam size during a crossing, the gap develops again after the crossing, since the voltage V_1 is still not equal to V_0 and $\langle n_2 \rangle \neq n$, as can be seen in Fig. 3. For example, in case $n = 0.137$, after crossing the 0.126 resonance, we have $\langle n_2 \rangle \approx 0.126$, therefore (from Eq. (27)), $V_1 \approx 18.9$ kV, $V_0 = 24$ kV.

8. Electric field correction

The basic influence of the electric field in the $(g-2)$ experiment, without taking into account muon vertical oscillations, is two-fold. On one hand, a radial component of the electric field in the lab-system produces the corresponding part of the vertical magnetic field in the muon rest frame and, therefore, changes the spin rotation frequency. On the other hand, the same component of the electric field changes the muon revolution frequency in the lab-system and hence the rotation frequency of the muon momentum. These two changes have the same sign, so the frequency of the muon spin rotations relative to its momentum rotations depends on the difference between these two effects, as is evident in the basic formula for the muon spin precession frequency observed in the lab-system:

$$\vec{\omega}_a = -\frac{e}{mc}\left[a\vec{B} - \left(a - \left(\frac{m}{p}\right)^2\right)\vec{\beta} \times \vec{E}\right]$$
$$\beta = v/c. \qquad (35)$$

According to Eq. (35), the ideal ("magic") muon momentum is defined as $p_m = m/\sqrt{a} \cong$

Table 11
$\alpha(n)$ and $F(n)$ (see text) resulting from the discrete nature of the quadrupole structure in the $(g-2)$ ring

n	0.121	0.123	0.125	0.127	0.129	0.131	0.133	0.135	0.137	0.139
$\alpha(n)$	1.136	1.139	1.142	1.144	1.147	1.149	1.152	1.155	1.157	1.160
$F(n)$	0.994	0.993	0.992	0.992	0.991	0.992	0.992	0.992	0.992	0.991

3.094 GeV/c. When $p = p_m$, the coefficient before $\vec{\beta} \times \vec{E}$ in (35) equals zero. Moreover, in the ideal ring, the ideal muon-with magic momentum and with no betatron oscillations around the equilibrium orbit-is moving along the central orbit where $E = 0$. And though free betatron oscillations around this central orbit change the average momentum and the average electric field, these changes are negligibly small. That means that, with respect to the error caused by the electric field, only deviations from the magic momentum matter.

As a result of a distribution of the muon momenta and therefore their energies, equilibrium radii and revolution frequencies around their magic values, we have a systematic shift which follows from Eq. (35):

$$\frac{\Delta\omega_a}{\omega_a} = -2F(n)n(1-n) \times \left[\left\langle\left(\frac{f-f_m}{f_m}\right)^2\right\rangle + \left\langle\frac{f-f_m}{f_m}\right\rangle\frac{f_m-f_0}{f_m}\right]. \quad (36)$$

In this formula, $f = v/2\pi R$ is the muon revolution frequency, f_m its magic value, f_0 its value at a radius R_0 where $E = 0$; and terms proportional to $\Delta v/v = (1-\beta^2)\Delta p/p \equiv \Delta p/p\gamma^2 \ll \Delta p/p$, are neglected, where $\beta = v/c$ and $\Delta R/R = -\Delta f/f$. As for $F(n)$, $F(n) \sim 1$, this is the factor correcting the small inaccuracy of the "smooth" approximation which is used without taking into account the actual structure of the focusing electric field along the ring:

$$F(n) = \frac{n_0}{n(1-n)\alpha^2}\frac{2}{\pi}\left[\frac{l_q/R}{1-n_0} + \frac{2}{\sqrt{1-n_0}}\left(\frac{D_{\min}(n)}{R} - \frac{1}{1-n_0}\right) \times \sin\left(\sqrt{1-n_0}\,\frac{l_q}{2R}\right)\right] \quad (37)$$

$$\alpha = \frac{2}{\pi}\left[\frac{l_q/R}{1-n_0} + \frac{2}{\sqrt{1-n_0}}\left(\frac{D_{\min}}{R} - \frac{1}{1-n_0}\right) \times \sin\left(\sqrt{1-n_0}\,\frac{l_q}{2R}\right) + \frac{l_i}{R} + 2\left(\frac{D_{\max}}{R} - 1\right)\sin\frac{l_i}{2R}\right] \quad (38)$$

$$\alpha = \left\langle\frac{D(s)}{R}\right\rangle; \quad \frac{\langle R_e(s)\rangle - R_0}{R_0} = \alpha\frac{p-p_0}{p_0}. \quad (39)$$

The averaging in Eq. (39) is made along a muon equilibrium trajectory. The quantities α and $F(n)$ are given in Table 11.

We see that with a very good accuracy 0.4% we can put $F(n) = 1$ in Eq. (36) for any n from Table 11. To correct [3,1] for the systematic shift estimated in Eq. (36) we need to measure n, and the revolution frequency distribution as described in Ref. [21]. The electric field correction in E821 is $\sim$0.5 ppm.

9. Conclusion

We described the design, construction and performance of the quadrupole system, its dimensions and parameters related with the $(g-2)$ experiment. For the same field focusing index the electric field gradient for the BNL E821 experiment had to be 1.7 times larger than that of the last CERN muon $(g-2)$ experiment. Even so, our quadrupole lead design quenches the low energy electron trapping making possible the construction of a dependable quadrupole system. It also allowed for the application of DC high voltage on the plates making possible the measurement of the axial oscillation frequency of the trapped electrons which relates to the electric field strength inside the quadrupole region. The application of the DC high voltage helped eliminate

the systematic error on the B-field due to the circulating trapped electrons.

Acknowledgements

During the quadrupole construction and maintenance of the system many excellent technicians worked with dedication on the project. In particular we wish to thank Augi Hoffman, Robert Wheeler from BNL and Ralf Ziegler from Heidelberg University for their excellent technical skills and ingenious work during construction. Many thanks to Joseph Yelk for his tireless efforts constructing many versions of the high voltage switches during the R&D period. The quadrupole plates were first glued together, but it turned out the sheer strength of the glue was not perfect and some of them snapped out when moved. The 1997 run was performed with most of the quadrupole plates glued while three of the plates had screws. For all the other runs they were all retrofitted with screws. John Benante, Steve Kochis, and Don von Lintig are greatly appreciated for their precision skills in re-mounting the quadrupole plates using screws, and for positioning and measuring the quadrupole plates locations to better than ± 0.5 mm with respect to the magnet pole pieces.

We also thank Derek Lowenstein, Phil Pile and the staff of the Accelerator Department for their help and support in the planning and construction of this device. Erik B. Forsyth suggested the use of Thyratron tubes as reliable high voltage switches and we are grateful to him for it. Arlene Wu Zhang designed the reliable electrical circuits of the Thyratron triggers. Wuzheng Meng's invaluable help with OPERA is greatly appreciated.

Finally we appreciate G. Townsend Zwart's help during the early stages of R&D. Larry Leipuner suggested the design of the home made high voltage monitors resulting to substantial savings. Last but not least we thank Ernst Sichtermann for reading the paper and making many helpful comments.

References

[1] G.W. Bennett, et al., Phys. Rev. Lett. 89 (2002) 101804 e-Print Archive: hep-ex/0208001, and references therein.
[2] G.T. Danby, et al., Nucl. Instr. and Meth. A 457 (2001) 151.
[3] J. Bailey, et al., Nucl. Phys. B 150 (1979) 1.
[4] V. Bargmann, et al., Phys. Rev. Lett. 2 (1959) 435.
[5] J.D. Jackson, Classical Electrodynamics, 2nd Edition, Wiley, New York, 1975.
[6] R. Prigl, et al., Nucl. Instr. and Meth. A 374 (1996) 118.
[7] X. Fei, et al., Nucl. Instr. and Meth. A 394 (1997) 349.
[8] H. Wiedemann, Particle Accelerator Physics, Springer, Berlin, 1993.
[9] E. Benedict, et al., Beam Dynamics in the Muon ($g-2$) Ring, Nucl. Instr. and Meth., submitted for publication.
[10] E. Efstathiadis, et al., Nucl. Instr. and Meth. A 496 (2003) 8.
[11] A. Grossmann, Magnetic field determination in a superferric storage ring for a precise measurement of the muon magnetic anomaly, Dissertation, University of Heidelberg, 1998, unpublished.
[12] R.C. West, et al. (Eds.), Handbook of Chemistry and Physics, 65th Edition, Chemical Rubber Co., 1984–1985.
[13] S. Sedykh, et al., Nucl. Instr. and Meth. A 455 (2000) 346.
[14] W. Flegel, F. Krienen, Nucl. Instr. and Meth. 113 (1973) 549.
[15] L. Brown, G. Gabrielse, Rev. Mod. Phys. 58 (1986) 233.
[16] B.L. Roberts, et al., Muon ($g-2$) (E821) Design Report, 3rd Edition, March 1995.
[17] OPERA, Electromagnetic fields analysis program, Vector Fields Ltd., 24 Bankside, Oxford OX5 1JE, England.
[18] High voltage storage capacitors, model RC1207 from RFI Corp., 100 Pine Aire Drive, Bay Shore, L.I., N.Y. 11706.
[19] English Electric Valve, Waterhouse Lane, Chelmsford, Essex CM1 2QU, England.
[20] Glassman High Voltage, Inc., Route 22 (East), Salem Industrial Park, P.O. Box 551, Whitehouse Station, NJ 08889, USA.
[21] Y. Orlov, C.S. Ozben, Y.K. Semertzidis, Nucl. Instr. and Meth. A 482 (2002) 767.